

**$\text{Na}_{0.66}(\text{Ni}_{0.13}\text{Mn}_{0.54}\text{Co}_{0.13})\text{O}_2$ Cathode Coated with Alucone by Molecular Layer Deposition
for Sodium Ion Batteries**

by
Justin Raimbault

A thesis
presented to the University of Waterloo
in fulfillment of the
thesis requirement for the degree of
Master of Applied Science
in
Chemical Engineering

Waterloo, Ontario, Canada, 2018

© Justin Raimbault 2018

Author's Declaration

I hereby declare that I am the sole author of this thesis. This is a true copy of the thesis, including any required final revisions, as accepted by my examiners.

I understand that my thesis may be made electronically available to the public.

Abstract

The importance of batteries has skyrocketed in the twentieth century due to an impending energy crisis arising from a dependence on fossil fuels. Global warming has alerted the world to the environmental dangers of fossil fuel reliance and has spurred the development of clean energy sources. Clean energy sources are often less predictable and controllable than fossil fuel energy and require a means of storing energy until its use is required. The spreading growth of the electric vehicle industry has also spurred much research into high-performance batteries. Thus, batteries play an integral role in our everyday lives and are required for an environmentally-conscious future.

Lithium ion batteries currently dominate the portable battery industry due to their long lifetime, good capacity, and wide operating window. However, mineable sources of lithium are unsustainable in the long term and their expense, combined with the expense of the cobalt used in commercial cathodes, is a major barrier to widespread adaption of batteries for energy storage and electric vehicles. On the other hand, sodium is much more abundant and inexpensive than lithium, and its electrochemical behaviours are very similar to those of lithium. Thus, much time and effort are being invested into developing sodium ion batteries (SIBs) to replace lithium ion batteries.

One problem with many sodium ion battery cathodes is their instability at high voltages. These cathode materials undergo a phase change above 4.3 V which limits their energy density. To solve this problem, a coating can be applied to the cathode particles which prevents side reactions with the electrolyte, dissolution of active materials, and breakdown due to volume changes. Several coating methods could be used to accomplish this, but only atomic/molecular layer deposition can create the ultrathin, homogeneous, and defect-free coatings necessary for high performance SIBs. This thesis work investigates the effect of coating alucone, an alumina containing ethane linkers,

deposited by molecular layer deposition on the SIB cathode $\text{Na}_{0.66}(\text{Ni}_{0.13}\text{Mn}_{0.54}\text{Co}_{0.13})\text{O}_2$ (NaNMC). This work also details the optimization of the NaNMC cathode with regards to annealing temperature and chelating agent addition.

The research described in this thesis shows that an annealing temperature of 850 °C produced the purest crystal structure as observed from XRD and by testing its electrochemical performance. The addition of a chelating agent stabilized the metal ions in solution during synthesis and decreased the agglomeration of the particles after annealing. Specifically, the addition of citric acid resulted in the highest capacity and rate performance when the synthesized cathode material was fabricated into a coin cell, compared to other chelating agents tested.

After the optimization of the cathode material was completed, 5, 10, or 20 layers of alucone were coated onto assembled cathodes and their performance at a higher voltage of 4.5 V was compared to a pristine cathode of the same material. The cathodes with 10 and 20 layers of alucone had similar capacities to the pristine sample after 100 cycles of charge/discharge, but the sample with 5 layers of alucone had 20 mA h g⁻¹ (27%) more capacity than the pristine sample after 100 cycles. All coated samples had much better rate performances than the pristine sample, especially at 5 C and 10 C, and the 5-layer sample again outperformed all others. Electrochemical impedance spectroscopy revealed that the 5-layer sample had the lowest internal resistance which explains its superior rate performance. It also revealed that after 100 charge/discharge cycles up to 4.5 V, the 5-layer sample's resistance remained unchanged while the pristine sample's internal resistance more than doubled, indicating the alucone coating's excellent ability to stabilize the cathode at high voltages. The increased capacity and rate performance of the 5-layer sample also demonstrates its effectiveness at stabilizing the NaNMC cathode by preventing dissolution into the electrolyte, side reactions, and particle breakdown due to volume changes.

This work presents a simple method for increasing a cathode's cycle life and rate performance by depositing alucone using molecular layer deposition. While the alucone coating presented here was applied to an NaNMC cathode material it could likely find applications with other types of electrode materials.

Acknowledgements

I would first like to thank my wife Danielle for all her support and encouragement throughout this degree. I would also like to thank and acknowledge my parents Bev and Pierre for instilling a value for education in me and enabling me to pursue whatever paths I wanted.

Special thanks go to Dr. Yuanli Ding and Dr. Xiaolei Wang for their guidance and support on my projects, and to Ruilin Liang for his friendship. I also thank Dr. Aiping Yu for providing additional lab space and equipment for my experiments. Finally, I thank my supervisor Dr. Zhongwei Chen for his guidance during this process.

Table of Contents

Author's Declaration	ii
Abstract.....	iii
Acknowledgements.....	vi
List of Figures.....	x
List of Tables	xii
List of Abbreviations	xiii
List of Symbols.....	xv
1 Introduction	1
1.1 Thesis Organization	3
2 Background	4
2.1 Electrochemistry and Current Batteries	4
2.2 Battery Technology.....	5
2.2.1 Performance Quantification.....	5
2.2.2 Battery Composition.....	5
2.3 Lithium Ion Batteries	6
2.3.1 LIB Cathodes.....	8
2.4 Sodium Ion Batteries.....	13
2.4.1 Electrode mechanisms	14
2.4.2 Electrolyte.....	17

2.4.3	SIB Anodes	17
2.4.4	SIB Cathodes	23
2.4.5	NMC Materials	26
2.5	Coating.....	28
2.5.1	Atomic Layer Deposition	28
3	Characterization Methods	32
3.1	X-Ray Diffraction (XRD).....	32
3.2	Scanning Electron Microscopy (SEM)	33
3.3	Transmission Electron Microscopy (TEM)	35
3.4	Thermogravimetric Analysis (TGA).....	36
3.5	Inductively Coupled Plasma Atomic Emission Spectroscopy (ICP-AES)	36
3.6	Battery Cycling	37
3.7	Electrochemical Impedance Spectroscopy (EIS).....	38
4	Synthesis and Characterization of NaNMC	40
4.1	Temperature Optimization	40
4.2	Chelating Agent Optimization	43
4.2.1	Synthesis and Characterization of Final Composition	45
5	MLD Coating and Results.....	48
5.1	MLD Coating and Characterization.....	48
5.2	Electrochemical Characterization	50

6	Conclusions and Future Work.....	57
	References.....	60

List of Figures

Figure 1: Schematic of a simple electrochemical cell.	4
Figure 2: Operation of a lithium ion battery. ¹	7
Figure 3: Main classes of LIB cathodes. ⁵	10
Figure 4: The three mechanisms for LIB and SIB electrodes. ¹⁶	16
Figure 5: Popularity of solvents, salts, and additives used for SIB electrolytes. ¹⁴	17
Figure 6: Working potential and specific capacities of SIB anodes. ¹⁴	18
Figure 7: Interlayer spacing in carbon anodes and its effect on ion intercalation. ²⁰	19
Figure 8: Crystal structures of a) rutile and b) anatase TiO ₂ with the red spheres representing oxygen atoms. ²⁰	20
Figure 9: Comparison of cycle performance for anatase and rutile TiO ₂ , both pristine and doped with Nb. Black traces represent commercial TiO ₂ samples with larger particle sizes. ²⁰	21
Figure 10: Simulation showing effect of Sn initial particle size on mechanical stability after reacting with Na. ⁵⁹	22
Figure 11: Working potential and specific capacities of SIB cathodes. ¹⁴	23
Figure 12: Illustration of O3- and P2-type layered oxide cathodes. ¹⁴	24
Figure 13: Schematic of ALD mechanism with TiCl ₄ and H ₂ O as the precursors. ⁹⁴	29
Figure 14: Reaction mechanism of MLD of alucone using trimethylaluminum and glycerol. ¹⁰⁵	31
Figure 15: Bragg's diffraction of X-rays in crystal lattice planes. ¹¹⁰	32
Figure 16: Components of a SEM. ¹¹¹	34
Figure 17: Nyquist plot of a typical EIS measurement on a half-cell battery assembly. ¹¹²	38
Figure 18: TGA of the viscous metal acetate solution.....	41

Figure 19: XRD spectra of NaNMC annealed at 800, 850, or 900 °C. The asterisks (*) denote extra peaks possibly belonging to NaMn_2O_4 .	42
Figure 20: a) Capacity at 1 C and b) rate performance of NaNMC annealed at three different temperatures.	43
Figure 21: XRD spectra of NaNMC samples synthesized with various chelating agents: citric acid (CA), ascorbic acid (AsA), glycolic acid (GA), and adipic acid (AA).	44
Figure 22: a) Rate performance from 2-4.3 V and b) cycle life from 2-4.3 V at 0.5 C of NaNMC synthesized with various chelating agents.	45
Figure 23: XRD of as-synthesized NaNMC compared to PDF No:27-0751.	46
Figure 24: SEM image of as-synthesized NaNMC microflakes.	47
Figure 25: Reaction mechanism of MLD of alucone using trimethylaluminum and glycerol. ¹⁰⁵	49
Figure 26: TEM image of NaNMC (dark) with 50 cycles of alucone coating by MLD.	49
Figure 27: Uncoated NaNMC cycled at 1 C from 2 V to 4.3, 4.4, or 4.5 V.	51
Figure 28: Cycle performance of NaNMC with 0, 5, 10, or 20 layers of alucone deposited by MLD. Cells were cycled at 0.5 C from 2-4.5 V.	52
Figure 29: Voltage profiles for the first cycles of NaNMC coated with 0, 5, 10, or 20 layers of alucone at a current of 0.5 C.	53
Figure 30: Rate performance of NaNMC coated with alucone. Voltage range for all samples was 2-4.5 V.	54
Figure 31: EIS of NaNMC coated with different layers of alucone a) before charge/discharge cycling and b) after 100 cycles at 0.5 C from 2-4.5 V in a typical coin cell setup.	55
Figure 32: Long-term cycling performance of NaNMC with 5 layers of alucone cycled between 2.0 V and 4.50, 4.55, 4.60, or 4.65 V.	56

List of Tables

Table 1: Differences between lithium and sodium relevant to use in batteries.	14
Table 2: Elemental composition of NaNMC from ICP-AES	46

List of Abbreviations

AA	Adipic Acid
ALD	Atomic Layer Deposition
AsA	Ascorbic Acid
C	Chare/discharge rate; 1 C = charge/discharge in 1 hour
CA	Citric Acid
d	Interlayer spacing
DEC	Diethyl Carbonate
EC	Ethylene Carbonate
EIS	Electrochemical Impedance Spectroscopy
FEC	Fluoroethylene Carbonate
GA	Glycolic Acid
GO	Graphene Oxide
ICP	Inductively Coupled Plasma
kV	Kilovolt
LIB	Lithium Ion Battery
mA h g ⁻¹	Milliamp hours per gram (capacity)
MLD	Molecular Layer Deposition
n	An integer
nm	Nanometer (length)
NMC	Class of material with Ni, Mn, and Co
PDF	Powder Diffraction File
rGO	Reduced Graphene Oxide
SEM	Scanning Electron Microscopy
SHE	Standard Hydrogen Electrode
SIB	Sodium Ion Battery
TEM	Transition Electron Microscopy
TGA	Thermogravimetric Analysis
TMO	Transition Metal Oxide
V	Voltage

W h g ⁻¹	Watt hours per gram (energy density)
W kg ⁻¹	Watts per kilogram (power density)
XRD	X-Ray Diffraction

List of Symbols

$^{\circ}\text{C}$	Degrees Celsius
μm	Micrometer (length)
\AA	Angstrom (length)
Z'	Real resistance
Z''	Imaginary resistance
θ	Diffraction angle
λ	Wavelength
Ω	Ohm (resistance)

1 Introduction

Humankind's widespread use of and dependence on fossil fuels over the last century has led to a significant impact on the environment, known as climate change. The pressure to reduce this negative effect on our planet, coupled with the decreasing supply of fossil fuels, has driven a scientific search for renewable energy sources and a societal shift to accept and promote these renewable energies. However, modern renewable energies such as solar, wind, and geothermal energies are unreliable in that their supply does not always match demand. One solution to this is to use large-scale rechargeable batteries to store energy when it is produced but not needed and release this energy when the energy demand surpasses production. Thus, there exists a need in the scientific community to develop low-cost batteries with high energy densities for large-scale energy storage.

The shift from fossil fuels to renewable energies has also impacted the transportation industry. The demand for electric vehicles (EVs) that run on electricity instead of fossil fuels has increased dramatically over the last decade, and the biggest challenge for EVs is the battery system. The main drawback to EVs is the short driving range which is limited by the EVs' batteries. Advanced rechargeable batteries with high capacity but low weight and volume are desperately needed before EVs can have a significant share in vehicle markets compared to conventional fossil fuel-based vehicles, and this drives scientific advancement in mid-scale battery applications.

Advanced batteries are also needed to power portable electronics which play a very large role in our society's current lifestyle. Cell phones, laptops, medical devices, and innumerable other electronic gadgets depend on batteries with high capacity, fast charging and discharging, and long cycle life, among other properties. Development of new materials for these small-scale batteries is widely pursued by researchers around the world.

It is clear from these large-, medium-, and small-scale examples that research into next-generation rechargeable batteries would benefit many people across many areas of life. The current gold standard for rechargeable batteries is the lithium ion battery (LIB), which was first developed by Sony in 1991 and is now common in many devices. While the LIB has met this generation's requirements, its high cost is driving research into next-generation batteries. One of these new types is the sodium ion battery (SIB), which has a reaction mechanism similar to that of an LIB but is cheaper due to sodium's abundance in nature. SIB technology is still in its developing stage and one problem that still must be overcome include the electrode materials' low stability at higher operating voltages, reducing the battery's total energy density.

This thesis aims to optimize the synthesis of an LIB cathode belonging to the NMC class: that is, a sodium oxide with nickel, manganese, and cobalt. The specific composition of the cathode synthesized in this thesis is $\text{Na}_{0.66}(\text{Ni}_{0.13}\text{Mn}_{0.54}\text{Co}_{0.13})\text{O}_2$, which will be referred to as NaNMC for the remainder of this thesis while the material class will be referred to as simply NMC. In addition, this thesis will show the merits of coating an organic-metal hybrid material called alucone on this NaNMC cathode by molecular layer deposition (MLD) and explore the effect of coating thickness on battery performance. To fulfill the first objective, the effect of annealing temperature and presence of various chelating agents during synthesis of $\text{Na}_{0.66}(\text{Ni}_{0.13}\text{Mn}_{0.54}\text{Co}_{0.13})\text{O}_2$ will be explored. To fulfill the second objective, an ultrathin alucone layer of 5, 10, or 20 MLD cycles will be coated on the optimized electrode and its effect on half-cell battery performance will be evaluated using a variety of techniques.

1.1 Thesis Organization

Section 2 of this thesis will describe the fundamental operating principles of batteries, focusing on LIBs and SIBs. Basic concepts such as the shuttling mechanism, charge/discharge, capacity, and potential will be reviewed. The motivation for shifting from LIBs to SIBs will be explained and a review of the electrolyte, anode materials, and cathode materials used in SIBs will be presented. The last part of Section 2 will go into the details of NMC materials used for cathodes in SIBs.

Section 3 will cover all of the characterization methods used for obtaining this thesis's results. This includes physical characterization techniques, such as TGA and XRD, as well as electrochemical characterization methods, such as charge-discharge cycling and electrochemical impedance spectroscopy.

Section 4 explains the motivation for using $\text{Na}_{0.66}(\text{Ni}_{0.13}\text{Mn}_{0.54}\text{Co}_{0.13})\text{O}_2$ as a cathode material and the procedures used to optimize its synthesis. Specifically, the relationship between annealing temperature, crystal structure, and battery performance will be explored, as well as the presence of various chelating agents during the first part of the synthesis.

Section 5 contains the main goal of this thesis: to demonstrate the benefits of coating alucone on $\text{Na}_{0.66}(\text{Ni}_{0.13}\text{Mn}_{0.54}\text{Co}_{0.13})\text{O}_2$ using molecular layer deposition and explore the effects of coating thickness on electrochemical performance. Coatings made with 5, 10, and 20 cycles of MLD will be compared to the pristine electrode using cell cycling and electrochemical impedance spectroscopy. Lastly, Section 6 will conclude the thesis and offer recommendations for further research based on the results from Section 5.

2 Background

2.1 Electrochemistry and Current Batteries

Electrochemistry is the study of the relationship between electrical and chemical processes and is the fundamental science behind the operation of batteries and fuel cells. Electrochemistry draws heavily from both chemistry and physics to explain the phenomena of this relationship. The most basic electrochemical unit is called an electrochemical cell and is made up of an ionic conductor sandwiched between two electronic conductors as shown in Figure 1 and the junction between an electronic and ionic conductor is called an electrode.

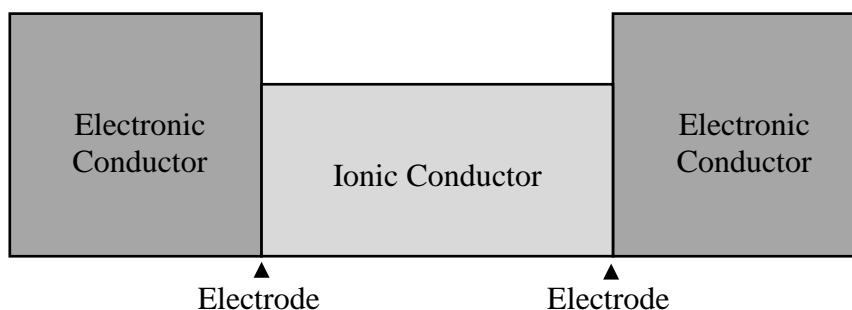


Figure 1: Schematic of a simple electrochemical cell.

If the two electronic conductors in an electrochemical cell are made of different materials, there could exist a difference in electrochemical activities which causes an electric potential difference. Chemical reactions can occur at these junctions, and the reaction which produces electrons is called oxidation and the electrode at which it occurs (during battery discharge) is called the anode. The reaction which consumes electrons is called reduction and occurs at the cathode. These two reactions enable electricity to pass from the electrodes to the electrolyte solution and vice-versa. As these two reactions proceed, the cell will eventually reach an equilibrium state as the electrochemical activities of the two electrodes become equal.

2.2 Battery Technology

Batteries, used as power sources, fall into one of two categories. Primary batteries are non-rechargeable and are designed to be discarded when its active materials are depleted, while secondary batteries are rechargeable. Both types of batteries strive to minimize internal resistance and maximize power output and thus electrolytes are selected to have high conductivity. Liquid electrolytes usually require a thin, porous, and inert separator to prevent electrode-electrode contact. Since the active materials in each electrode may not have a very high conductivity, they are often plated on a metallic grid and mixed with carbon to increase overall conductivity.

2.2.1 Performance Quantification

The performance of batteries and their individual components is quantified through a variety of measurements. For example, capacity is the amount of electricity that a battery can provide before it is depleted and is usually measured in mA h g^{-1} . A higher capacity means that a battery can last longer before needing to be recharged. The energy density of a battery is the total electrical energy that can be delivered and can be reported in units of W h g^{-1} . Another criterion that is useful in applications where short bursts of power are needed, such as starting a car, is power density, measured in W kg^{-1} . The number of times a battery can be charged/discharged without losing significant performance is called cycle life and is very important for applications such as laptops and cell phones which rely heavily on daily battery usage. The rate at which a battery is charged or discharged is measured by the current, in mA, or by C-rate, where 1 C is the current needed to charge or discharge a battery in 1 hour, 2 C will charge or discharge the battery in 0.5 hours, etc.

2.2.2 Battery Composition

The simplest type of active material in a battery's anode is metal, such as zinc. A metal with lower atomic weight can have higher specific energy and power density and thus lithium is a great

anodic material as it is the lightest metal. The drawback to using lithium is that it reacts violently with water, prohibiting the use of an aqueous electrolyte. The products of the anodic reaction are metals of a higher valence state, such as Zn^{II} or Li^I . The requirement for these products is that they must be either soluble in the electrolyte or form a porous structure so that the unreacted metal remains accessible. The cathode, on the other hand, is often composed of an oxide of a metal in a high oxidation state which decreases upon reaction.

For secondary batteries, which are rechargeable, the cathodic and anodic reaction products must remain close to their corresponding electrodes to stay available for the reverse reaction upon recharging. A complication arises from the fact that the reaction products are of different densities, causing the volume of the active materials to differ between the charged and discharged states. Since batteries are sealed, leaks due to this volume change must be prevented. Volume changes are often responsible for particle breakdown and loss of contact with the current collector as repeated cycling induces stress in the particle.

2.3 Lithium Ion Batteries

Although the final work of this thesis is an application for sodium ion batteries, SIBs and LIBs have much in common, including their operating mechanisms. In fact, most of the technological advances in the LIB field also apply to SIBs and have served to kickstart SIBs' research such that the current state of SIB technology, being approximately five years old, is much more advanced than that of LIBs during their early development. It is thus appropriate to first present an overview of LIB materials and technologies before moving to SIBs.

LIBs, invented about one hundred years after the lead-acid battery, use a different reaction mechanism than the first rechargeable batteries. The first LIB, proposed in the 1970s, consisted of

a titanium(II) sulfide cathode and a lithium metal anode. Since then, LIBs have been the focus of much scientific research to increase their capacity, specific energy, and cycle life while also reducing their weight and size. They remain very popular in applications where weight and size are important parameters such as in portable electronics. LIBs are so popular since lithium is the lightest metal element and can have a very high energy density. Current LIBs also have long cycle lives (>1000 cycles) and a low self-discharge rate, making them ideal for portable electronics after factoring in their light weight.

The typical LIB operates via an intercalation reaction between lithium ions and the anode/cathode. This mechanism is also known as a rocking horse or shuttle mechanism, since lithium ions shuttle back and forth between the anode and the cathode upon cycling, as shown in Figure 2.

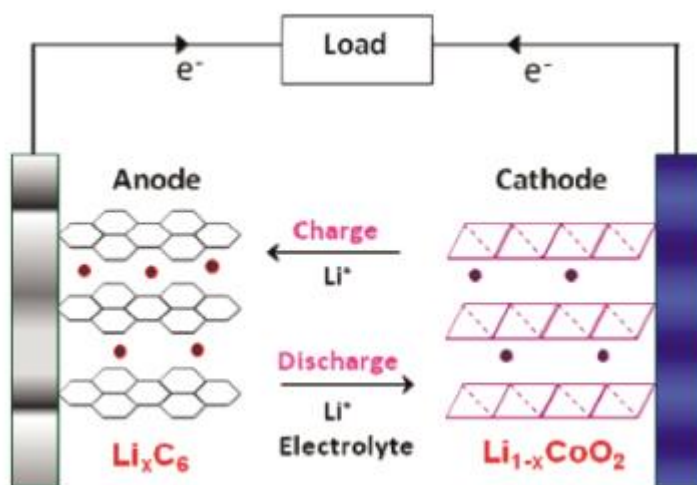
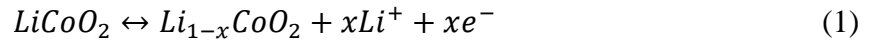


Figure 2: Operation of a lithium ion battery.¹

There are many materials available for use as electrolytes, anodes, and cathodes, but a typical LIB uses an anode made from an intercalated lithium compound instead of pure lithium, such as lithium in porous carbon, since pure lithium is more dangerous and forms dendrites upon extended cycling which can pierce through the separator and short the battery. The cathode can be made

from a layered lithium oxide such as lithium cobalt oxide. In LIBs, non-aqueous electrolytes must be used since lithium reacts vigorously with water and thus an organic carbonate combined with a lithium ion complex is usually used as the electrolyte. Example reactions for the cathode and anode, respectively, are shown below:



2.3.1 LIB Cathodes

Since the subject of this thesis work is an LIB cathode, and SIB materials and mechanisms are closely related to those of LIBs, an overview of LIB cathode materials will be helpful for setting the stage before detailing SIB cathode materials. Conversely, an overview of LIB anodes will not be as useful since it applies to a different type of battery and a different electrode. Further, the main anode material for LIBs is carbon-based, specifically graphite, and since the size of sodium ions is too large to be accommodated in this anode material without special considerations, it does not play a large role in SIB technologies. In the interest of brevity this section will not include LIB anodes and will instead summarize the four main classes of LIB cathodes: $LiCoO_2$, $LiFePO_4$, $LiMn_2O_4$, and $LiNiMnCoO_2$, which have 2D, 1D, 3D, and 2D ion diffusion pathways, respectively.

2.3.1.1 $LiCoO_2$

The first commercial LIBs used lithium cobalt oxide ($LiCoO_2$) as the cathode material.² When it was originally discovered that the lithium could be removed electrochemically, this material gained much attention as a potential LIB cathode and currently dominates the LIB market. $LiCoO_2$ has a 2D layered structure alternating between layers of CoO_2 and Li as shown in Figure 3. This results in a two-dimensional diffusion path for the Li ions which diffuse at a high rate of 5×10^{-9}

cm/s.³ This cathode material is typically cycled between the fully lithiated discharge state LiCoO_2 (3.0 V vs Li/Li^+) and a half-lithiated charge state Li_xCoO_2 (4.2 V vs Li/Li^+), where x ranges from 0.5 to 0.6.² If too much Li is extracted ($x < 0.5$), the crystal structure will rearrange irreversibly, resulting in a rapid capacity fade and low cyclability. The degradation of the crystal structure is due to the oxidation of some Co^{3+} atoms to Co^{4+} , which results in a contraction along the c -axis.

Because of the loss in performance at high deintercalation, LiCoO_2 cathodes have a capacity of only 130-150 mA h g^{-1} , roughly half of their theoretical capacity of 270 mA h g^{-1} .⁴ While this is high enough to be commercially successful, it is a bit low when compared to other cathode materials. Another disadvantage is that at high voltages, O_2 gas can be released from the transformed lattice and react with components of the electrolyte solution. Furthermore, the Li_xCoO_2 cathode also suffers from variable conductivity at different Li compositions. For example, at $x=0.6$ the cathode conducts like a metal but behaves like a semiconductor at $x=1$.³ LiCoO_2 is currently the most popular cathode material for LIBs because of the fast diffusivity of Li ions, useable capacity, and because it has been extensively studied. However, its structural deformation upon high Li extraction limits its cycle stability and its practical capacity, and its cost prohibits its use in large batteries. Recent improvements in its capacity have been made by coating LiCoO_2 with metal oxides, but the inherent 2D structure reduces the ion diffusion pathways.

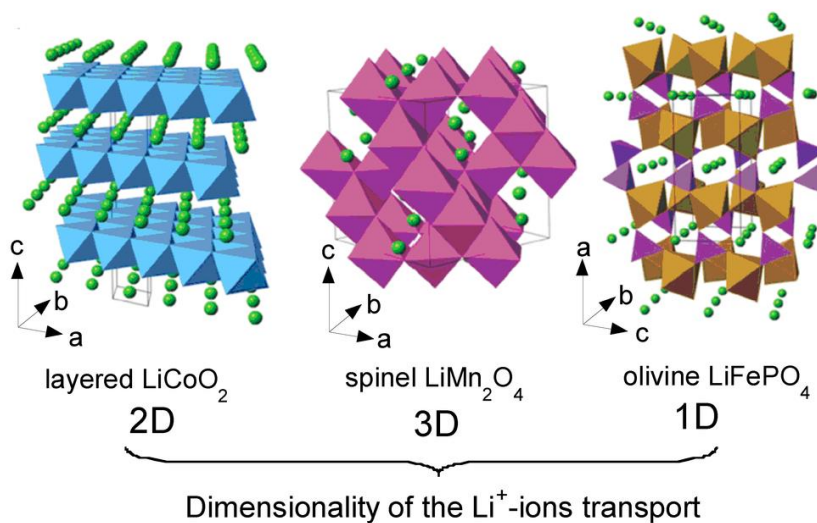


Figure 3: Main classes of LIB cathodes.⁵

2.3.1.2 LiFePO_4

Lithium iron phosphate in olivine phase was first proposed as a cathode material in 1997 by Padhi et al.⁶ This cathode material attracted much attention because it is made from abundant, low-cost elements and is environmentally friendly. Figure 3 shows the olivine crystal structure which promotes a 1D diffusion pathway for the Li ions. Its theoretical capacity is 170 mA h g^{-1} and in practice 100% capacity can be achieved. Additionally, it is very stable during charge/discharge and can cycle several hundred times without losing significant capacity. Other similar cathode materials in the same class include LiMPO_4 where M can be manganese, nickel, or cobalt. As of yet, these alternative compounds have not out-performed LiFePO_4 . LiFePO_4 also has the a lower voltage (3.4 V vs Li/Li^+) compared to other materials, reducing the possibility of side reactions with the electrolyte but decreasing its energy density.⁷

The main disadvantage of using LiFePO_4 as a cathode material is that it is a wide-gap semiconductor and has very low conductivity at room temperature. This can be overcome by a variety of techniques, the most popular of which employ a conductive carbon coating. This carbon

can be added in a gel form during synthesis or can be milled with the LiFePO_4 particles. Another strategy is to dope the cathode material with trace amounts of elements supervalent to lithium such as niobium, increasing the conductivity. Further potential solutions involve replacing a fraction of the Fe with Na, or O with N.² Another significant disadvantage is that its 1D structure results in a low rate.

2.3.1.3 LiMn_2O_4

The introduction of LiMn_2O_4 as a cathode material was first proposed by Thackeray et al. in 1983.^{8,9} LiMn_2O_4 exists in spinel form, which is a class of minerals with formula $\text{A}^{+2}\text{B}_2^{+3}\text{O}_4^{-2}$. This structure is shown in the middle image of Figure 3, which is also a good illustration for the differences in diffusion pathways for each of the three cathode materials introduced so far. The spinel structure of LiMn_2O_4 allows 3D diffusion of lithium ions, giving it the main advantage of having the highest rate performance when using a mesoporous form⁷. A and B can have different valences, such as $\text{Li}^{+1}\text{Mn}^{+3}\text{Mn}^{+4}\text{O}_4^{-2}$. In this case, the average valence state for the manganese is +3.5. Oxide anions are arranged in close-packed cubic structure and the A and B (or Li and Mn, in this cathode case) occupy the octahedral and tetrahedral locations. In $\text{Li}_x\text{Mn}_2\text{O}_4$, the composition can range in terms of lithium concentration from $0 < x < 2$. When $x < 1$, the structure is cubic, and when $x > 1$, the structure shifts to tetragonal. In the bulk state (no nanodomain structure), this structure shift results in the lack of good reversibility, but this can be avoided by using nanostructured LiMn_2O_4 , in which entire nanodomains can shift structures spontaneously.

Various nanoparticle forms of LiMn_2O_4 can be manufactured to increase cathode performance, such as nanowires. Smaller particles have a higher surface area to volume ratio, increasing their kinetics and rate capabilities due to enhanced contact between the particles and electrolyte. In particular, one group fabricated ultra-thin (5-10 nm diameter) LiMn_2O_4 nanowires

using solvothermal reaction to prepare MnO_2 nanowires followed by a solid-state reaction with LiOH .¹⁰ The major disadvantage to LiMn_2O_4 is that it has a lower capacity than LiCoO_2 or LiFePO_4 . Another downside is that LiMn_2O_4 suffers from self-discharge, especially at high temperatures, when using the electrolyte LiPF_6 due to the HF generated in the presence of moisture. This can be avoided by using different electrolyte such as LiBOB .³ Alternatively, substituting 2.5% of the Mn for Al , or coating the cathode surfaces with AlPO_4 which acts as a getter for HF , can solve the self-discharge problem.

2.3.1.4 *LiNiMnCoO₂*

The class of cathode material with the general formula LiNiMnCoO_2 , or Li(NMC)O_2 , was first reported in 2001 and promises to surpass the previous three materials in terms of battery performance. This material was first used in the form $\text{LiNi}_{1/3}\text{Mn}_{1/3}\text{Co}_{1/3}\text{O}_2$ and had a capacity of 150 mA h g^{-1} .¹¹ An initial capacity of 220 mA h g^{-1} was realized by increasing the charge cut-off voltage but capacity fade occurred. The synthesis of this compound was conducted at temperatures of around $800 \text{ }^\circ\text{C}$. Changing the ratio between the Ni , Mn , and Co elements changes the lattice parameters of the crystal structure, and much work has been conducted on synthesizing compounds with different element ratios. For example, it has been concluded that increasing the amount of cobalt reduces the amount of nickel ions in the lithium layer, while nickel is the electrochemically active component at low potentials. The structure is generally layered, enabling 2D ion transport, although there exists the possibility of a spinel structure at specific element ratios.

Although this material shows good electrochemical properties, it has low conductance, meaning that additives such as carbon must be used for a high-performing cathode. The material $\text{LiNi}_4\text{Mn}_4\text{Co}_2\text{O}_2$ had an improved capacity of 170 mA h g^{-1} and only showed a change in volume of 2% as lithium was removed.¹¹ This type of material has a higher storage capability and a higher

potential cutoff without losing capacity when compared to the current standard of LiCoO_2 cathodes. Still, optimization of the element ratios remains to be determined. For example, one group reported the synthesis and characterization of polycrystalline nanostructured $\text{Li}_{0.28}\text{Co}_{0.29}\text{Ni}_{0.30}\text{Mn}_{0.20}\text{O}_2$ which had a capacity of 200 mA h g^{-1} which faded to 138 mA h g^{-1} after 100 cycles.¹² Another group fabricated $\text{Li}[\text{Li}_{0.20}\text{Ni}_{0.16}\text{Co}_{0.10}\text{Mn}_{0.54}]\text{O}_2$ cathodes with a capacity of 226 mA h g^{-1} and 95% capacity retention after 50 cycles, a marked improvement over conventional LiCoO_2 cathodes.¹³ This demonstrates the possibility of increased performance of optimized LiNiMnCoO_2 cathodes.

2.4 Sodium Ion Batteries

The main problem with LIBs is that the world's current mineable supply of lithium is limited and is sustainable for only 65 more years.¹⁴ If the use of LIBs for large-scale energy storage becomes widespread the demand for lithium will climb rapidly and push the current price of \$5000/ton for lithium carbonate, the most common source of lithium, even higher.^{14,15} While recycling efforts may offset some of this cost if such programs develop alongside the expanding demand and use, the fact remains that the application of LIBs for grid energy storage and EVs is limited by lithium's high cost.

The high cost and bleak future prospects of lithium source depletion are driving research into replacing lithium with sodium since sodium carbonate, the main source of sodium, costs only \$150/ton compared to lithium carbonate's \$5000/ton.¹⁵ Sodium sources are extremely abundant since sodium is the fourth most common element in the earth's crust and sources are spread across the globe, including 23 billion tons of soda ash in the United States alone.¹⁵ This high availability and low cost, coupled with the many similarities between sodium and lithium, make SIBs an attractive and viable alternative to LIBs.

While sodium behaves very similarly to lithium in a battery, there are differences, summarized in Table 1, which prevent direct replacement of lithium with sodium. The biggest disadvantage to sodium is that its atomic radius is larger than that of lithium: 1.06 Å for sodium and 0.76 Å for lithium. This means that it is too large to fit into the interstitial sites of some electrode materials such as graphite. This is especially problematic since graphite is the most popular anode material for LIBs but cannot be used in SIBs. Its larger size also leads to a decrease in ionic mobility and slower reaction kinetics overall. Further, sodium has a slightly higher redox potential (-2.71 V vs. SHE) compared to lithium (-3.0 V vs. SHE), creating batteries with lower energy densities than their lithium counterparts.¹⁴ Sodium is also much heavier per mole than lithium and correspondingly has a lower capacity, though much of this disadvantage is insignificant in a full cell with current collectors, cell materials, and electrode materials which weigh much more than the active ions. Creative measures must be developed to combat these disadvantages.

Table 1: Differences between lithium and sodium relevant to use in batteries.

Category	Lithium	Sodium
Cation Radius (Å)	0.76	1.06
Atomic weight (g/mol)	6.9	23
E^0 (vs. Li/Li ⁺)	0	0.3 V
Capacity (m Ah g ⁻¹), metal	3829	1165
Cost, carbonates	\$5000/ton	\$150/ton

2.4.1 Electrode mechanisms

As with LIB electrode materials, there are three mechanisms by which SIB electrodes operate, illustrated in Figure 4. The most common mechanism, and the one that is currently used in the most popular LIBs, is intercalation. During intercalation, ions are inserted into vacant interstitial

sites in a pre-existing crystal structure without destroying the crystal structure. This process is reversible; when a battery is charged, ions deintercalate from the cathode and intercalate into the anode material, and the reverse occurs upon discharge. One restriction on intercalation is that the ions must be small enough to fit in the vacant interstitial sites which is why lithium can intercalate into graphite but sodium cannot. Intercalation reactions generally involve only one ion per molecular unit, as in the following example reaction for the anode material $\text{Na}_2\text{Ti}_6\text{O}_{13}$, where $x < 1$:



Because of this, intercalation electrodes generally have lower capacities, but are not plagued by troublesome issues such as large volume expansion. These electrodes can react homogeneously, where all reaction sites have equal reaction probabilities, or heterogeneously, where the material tends to fill up directionally. At a basic level, most intercalation electrodes should react by homogeneous intercalation, but there are always exceptions such as defects or diffusion limitations which prohibit truly homogeneous intercalation.

Another intercalation mechanism is alloying, which is most well-known for its role in the Li-S battery. Sodium and lithium ions can form alloys with other materials, creating a new material. Alloying electrodes are known for having very high capacities since more than one ion can react with each molecular unit as the reaction proceeds to completion. For example, tin can alloy with sodium in the following progression: $\text{Sn} \rightarrow \text{NaSn}_5 \rightarrow \text{NaSn} \rightarrow \text{Na}_9\text{Sn}_4 \rightarrow \text{Na}_{15}\text{Sn}_4$.

In this manner, the ratio of Na:Sn gradually increases from 0:1 to 15:4. Voltage-capacity profiles for this type of electrode show multi-step traces corresponding to each type of alloy as it forms. The biggest disadvantage to alloying electrodes is their volume change. The electrode's volume simply cannot stay constant with such a different elemental composition between the

single-element electrode and the full-step alloy. It is possible for these types of electrodes to reach 420% volume changes during cycling which quickly leads to electrochemical pulverization of the individual particles, loss of contact with the current collector, and a sharp decline in battery performance.¹⁴ To mitigate this volume expansion and contraction several strategies can be implemented, such as using nanoparticles which can accommodate more volume change before mechanical failure, incorporating a matrix element into the electrode, coating electrode particles with a flexible material, and careful selection of operation voltage range.

Lastly, conversion electrodes have one phase when desodiated, but two distinct phases upon sodiation. One example is Fe_3O_4 , which undergoes the following reaction with sodium:



It is clear that this reaction produces two distinct materials, Fe and Na_2O , which confirms the conversion mechanism. Conversion also causes large volume expansions, but the problem is not as severe as in the alloying mechanism. Conversion electrodes are still under development.

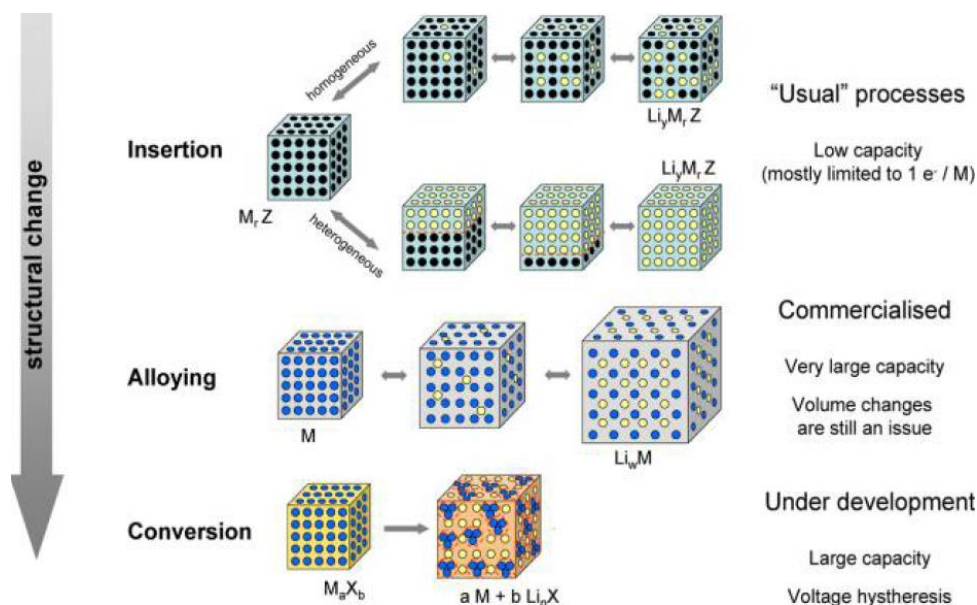


Figure 4: The three mechanisms for LIB and SIB electrodes.¹⁶

2.4.2 Electrolyte

The electrolyte used in SIBs is responsible for enabling the shuttle of sodium ions between the cathode and anode while preventing the diffusion of electrons. Other requirements include being chemically stable to avoid decomposition and electrochemically stable to avoid side reactions at high voltages. Low toxicity is also a benefit for real-world applications in case of cell failure. The electrolyte is comprised of a solvent, or combination of solvents, a salt of the shuttling ion, and optional additives. The solvent used in SIBs is typically propylene carbonate or a combination of ethylene carbonate and diethyl carbonate, while the most common salt is NaClO_4 followed by NaPF_6 . A common additive to the electrolyte solution is fluoroethylene carbonate which helps form a high-quality passivation layer on the electrode while suppressing unwanted reactions between the electrolyte and the active materials.¹⁴ Only 2-5% of this additive is needed to increase battery performance. A summary of the most-used solvents, salts, and additives is presented in Figure 5.

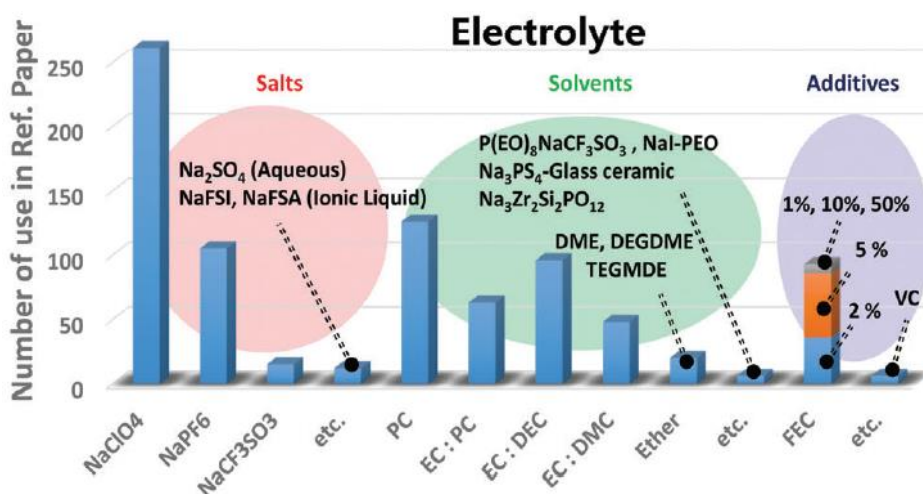


Figure 5: Popularity of solvents, salts, and additives used for SIB electrolytes.¹⁴

2.4.3 SIB Anodes

The following sections will review the classes of SIB anodes and use selected publications to demonstrate the current performance levels expected of SIB anodes, as well as what strategies are

being implemented to overcome problems and increase performance. A very thorough review paper published by Hwang *et al.* in 2017 provides a helpful summary of these materials, their operating voltages, and capacities, shown in Figure 6. The most promising materials in terms of capacity and low working potential are alloying anodes, such as P and Sn. Conversion transition metal oxides (TMOs) are clustered around 500 mA h g⁻¹ and 1 V, while intercalation TMOs have lower capacities around 175 mA h g⁻¹ and slightly lower potentials.

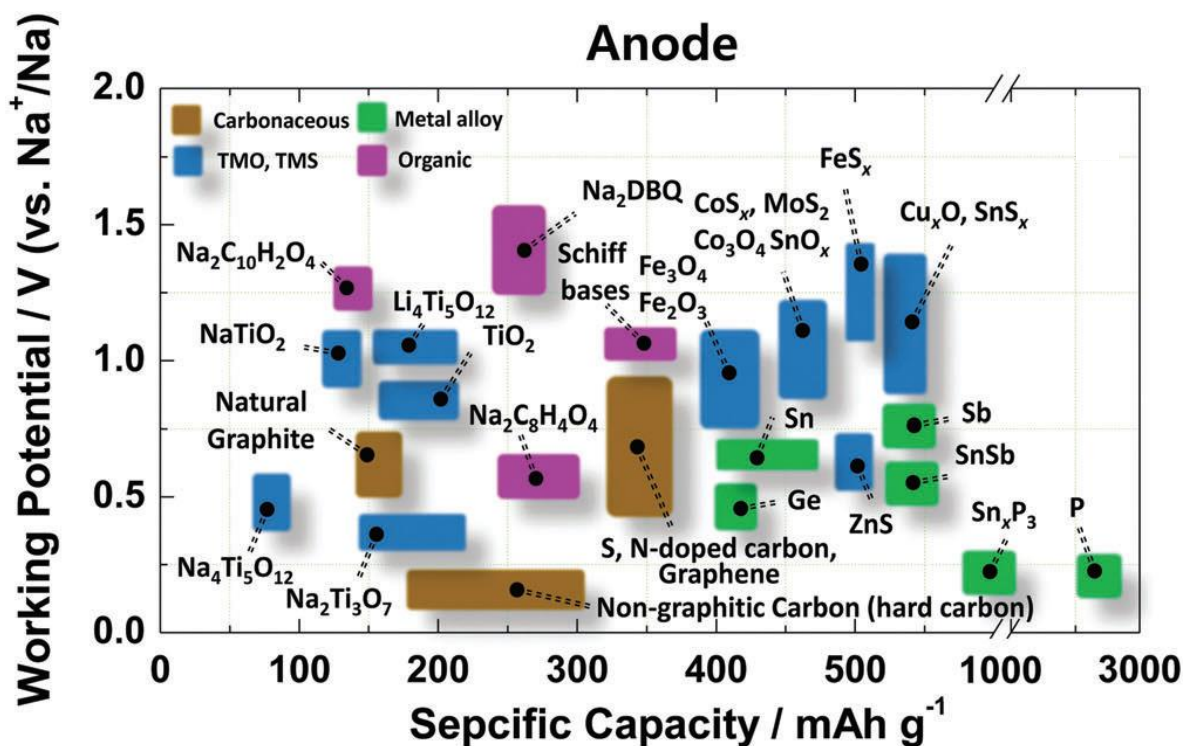


Figure 6: Working potential and specific capacities of SIB anodes.¹⁴

2.4.3.1 Intercalation

As was already mentioned, the most common type of intercalation electrode for LIBs is graphite, but sodium ions' larger size prevents their intercalation between graphite sheets. Instead, hard carbon, or non-graphitized carbon, can be used as a carbon-based intercalation anode material.¹⁷⁻¹⁹ Carbon sheets in hard carbon have a “house of cards” structure instead of being

tightly stacked like those in graphite, as shown in Figure 7, and can accommodate sodium ions to provide capacity in a cell. Carbon-based anodes are still useable for SIBs if they do not contain a large percentage of graphite.

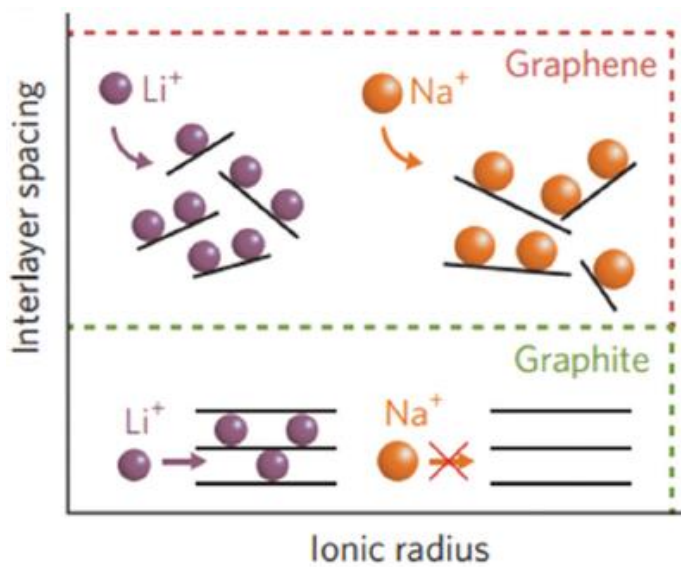


Figure 7: Interlayer spacing in carbon anodes and its effect on ion intercalation.²⁰

Graphene is a highly-explored material for SIB intercalation cathodes mainly due to its extremely high electronic conductivity and high capacity.^{14,15,20-23} Reduced graphene oxide (RGO), created by the thermal or chemical reduction of graphene oxide, can also be used as an anode material.²⁴⁻²⁶ The oxygen groups reduce conductivity but increase hydrophobicity, which simplifies synthesis and modification processes. One common modification for carbon-based electrode materials is heteroatom doping with boron, sulfur, or nitrogen. Substituting a heteroatom such as nitrogen into carbon sheets creates defect sites which have several benefits. These heteroatom defects form disordered carbon domains that improve anode stabilization, add active sites for increased capacity, and change carbon's electronic structure to increase the overall conductivity of the electrode.²⁷⁻³³

Titanium oxides have also been given attention as an LIB intercalation anode material due to their success in LIBs.^{34–38} TiO_2 is one such oxide and is used in two crystal forms: rutile and anatase. The crystal structure of each of these is shown in Figure 8.

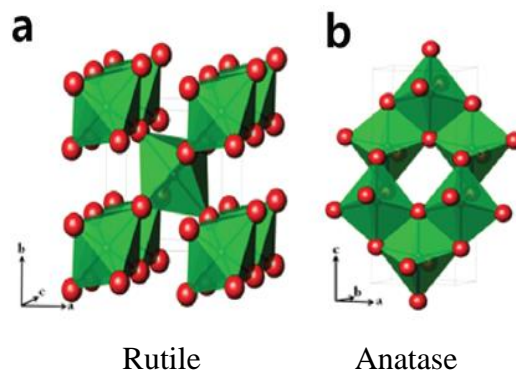


Figure 8: Crystal structures of a) rutile and b) anatase TiO_2 with the red spheres representing oxygen atoms.²⁰

Anatase TiO_2 usually performs better than rutile TiO_2 , with a higher initial capacity and better cycle life, but Usui *et al.* discovered that doping rutile TiO_2 with small amounts of Nb increases its performance past that of anatase TiO_2 .³⁸ The comparison between rutile and anatase TiO_2 , pristine and doped with Nb, is shown in Figure 9. Several conclusions can be drawn from this plot. First, the black traces represent commercial TiO_2 samples which had a larger particle size than the materials synthesized by Usui *et al.*, indicating that a smaller particle size increases the performance of electrode materials. This is likely due to more efficient insertion of Na ions into the interior of the active material particles. Second, while pristine anatase TiO_2 does perform better than pristine rutile TiO_2 , a small amount of Nb dramatically increases the performance of rutile TiO_2 while slightly decreasing the performance of anatase TiO_2 . The authors attribute this to a 3-magnitude improvement in electronic conductivity for rutile TiO_2 while anatase TiO_2 has slower Na^+ diffusion kinetics.³⁸

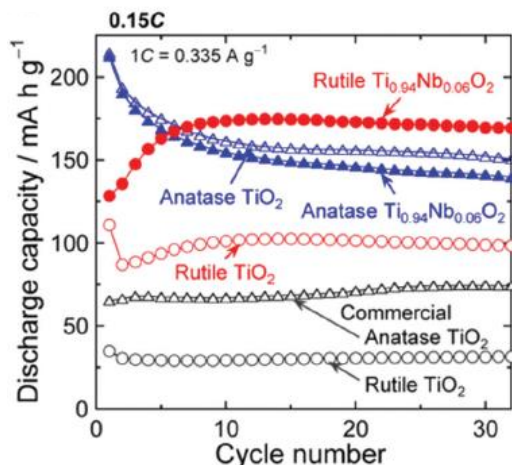


Figure 9: Comparison of cycle performance for anatase and rutile TiO₂, both pristine and doped with Nb. Black traces represent commercial TiO₂ samples with larger particle sizes.²⁰

Na₂Ti₃O₇ has also shown promise as an intercalation anode for SIBs as it has the lowest reported voltage for an oxide-based SIB anode.^{31,39,40} This material can accommodate two extra sodium ions as it cycles from Na₂Ti₃O₇ to Na₄Ti₃O₇, providing a theoretical capacity of 177 mA h g⁻¹. This is rather low compared to other anode materials, but its ease of synthesis and low working potential still prompt its investigation.

2.4.3.2 Conversion

Many transition metal oxides and sulfides fall under the category of conversion anodes for SIBs. While conversion anodes tend to have a higher capacity than intercalation anodes, they suffer from sluggish reaction kinetics and high volume expansion. Iron oxides, both Fe₃O₄ and Fe₂O₃,^{41,42} have been used, as well as Co₃O₄,⁴³ SnO₂,^{44,45} and CuO.^{46,47} Sulfides such as TiS₂,⁴⁸ FeS₂,⁴⁹ MoS₂,⁵⁰⁻⁵² and SbS⁵³ have also been reported. Sulfides are being investigated because the M-S bond, where M is a metal, is weaker than the M-O bond, which improves the kinetics of the conversion reactions.¹⁴

2.4.3.3 Alloying

Alloying SIB anodes have the highest reported capacities, especially phosphorous⁵⁴⁻⁵⁶ and tin^{45,57,58}. Their reaction pathways include multiple steps with progressively increasing ratios of Na to P or Sn, for example $\text{Sn} \rightarrow \text{NaSn}_5 \rightarrow \text{NaSn} \rightarrow \text{Na}_9\text{Sn}_4 \rightarrow \text{Na}_{15}\text{Sn}_4$. The biggest limitation of alloying materials is their very large volume expansion upon full reaction with Na. The reaction with Sn mentioned above has a volume expansion of 420%, which quickly leads to particle breakdown and loss of contact between the active material and the current collector.⁵⁹ Wang *et al.* simulated the volume expansion of Na_xSn to discover a 0.5 μm critical particle size below which particle breakdown is mitigated.⁵⁹ Particles this small will still eventually break apart after repeated cycling but that process will be much slower than if the particles were larger. Above a critical particle size of 1.6 μm , the Na_xSn particle cannot accommodate the stress caused by volume changes and becomes pulverized after the first cycle. Group 14 materials such as Ge⁶⁰ as well as Group 15 materials such as Sb^{61,62} and Bi⁶³ have also demonstrated the ability to react with Na as an anode material, but P and Sn are the most heavily researched.

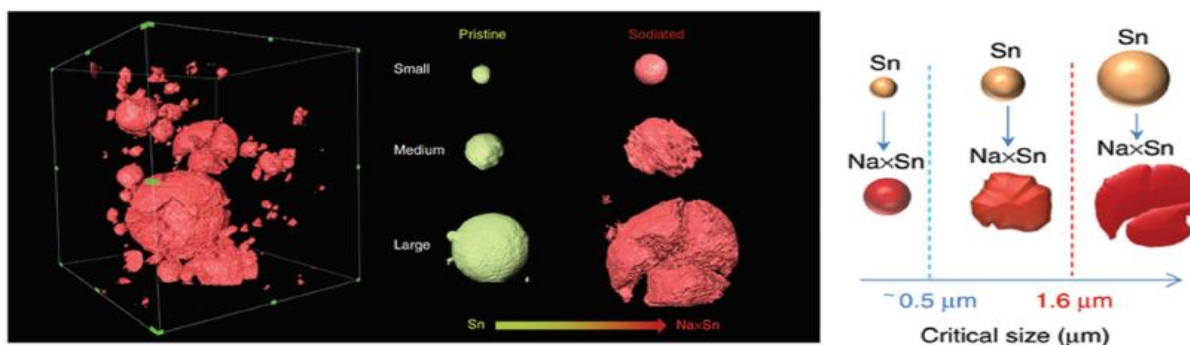


Figure 10: Simulation showing effect of Sn initial particle size on mechanical stability after reacting with Na.⁵⁹

2.4.4 SIB Cathodes

This section will be organized slightly differently than the section describing SIB anodes. TMO cathodes will be discussed first, which can be divided into O3-type and P2-type, followed by polyanionic cathodes, and lastly a more detailed explanation of the state-of-the-art NMC cathodes will be presented since this thesis work is on an NMC material. Intercalation-type cathode materials such as layered transition metal oxides, fluorides, phosphates including pyrophosphates and fluorophosphates, sulfates, and sodium superionic conductors have all been reported in SIBs.¹⁴ An overview of SIB cathode performance is shown in Figure 10. Layered P2-type cathodes have higher capacities than layered O3-type cathodes with the same operating voltage. Polyanionic compounds have a lower capacity which is counterbalanced by a higher working potential, increasing their energy densities. Organic and Prussian blue compounds are not well developed and will not be covered in this section.

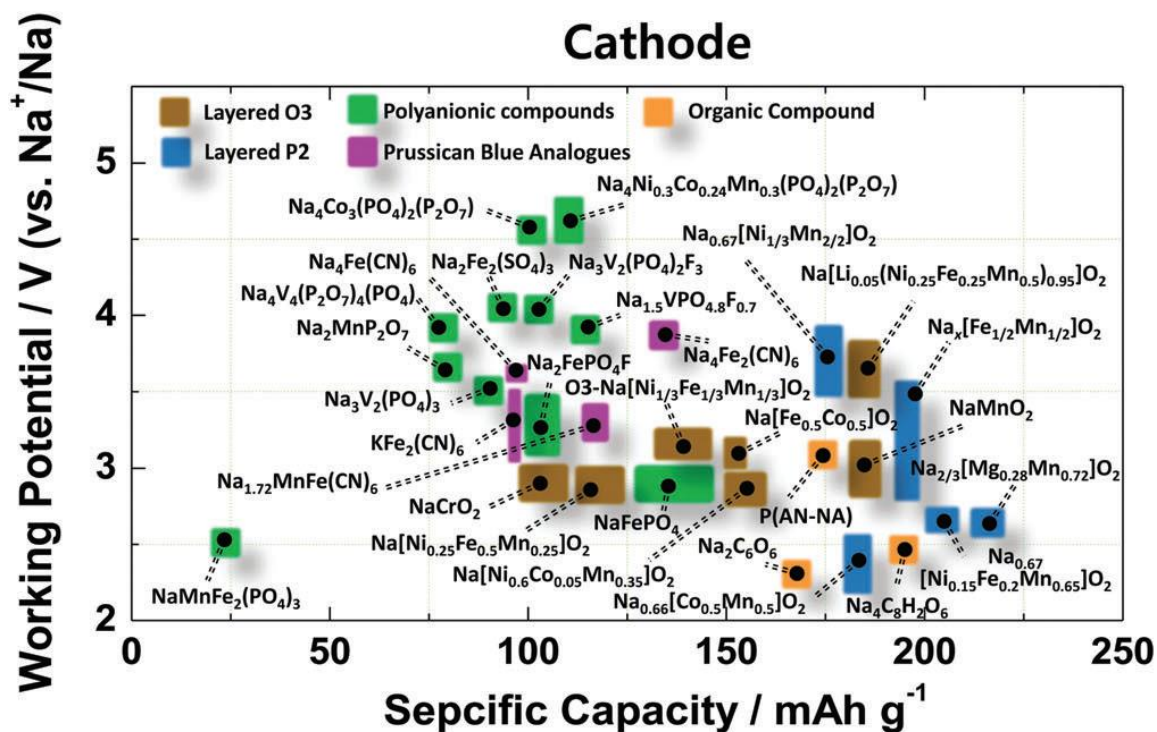


Figure 11: Working potential and specific capacities of SIB cathodes.¹⁴

2.4.4.1 Transition Metal Oxides

Transition metal oxides (TMOs) have garnered much attention as SIB cathodes due to their higher capacity, ease of synthesis, and similarities with established LIB cathodes. Layered TMO cathode materials can be divided into two main categories, O3 and P2, depending on the packing number of layers within each unit cell and whether the ion is located in an octahedral (O) or prismatic (P) environment (see Figure 12).⁶⁴ P2-type structures are stable in sodium-deficient compounds (when $x < 0.7$ in Na_xMO_2) since the absence of ions creates vacancies, increasing repulsion between oxygens and leading to a larger interlayer distance which allows faster sodium ions diffusion.¹⁴ P2-type cathodes also tend to have higher capacity and reduced slab gliding than O3-type cathodes. P2-type materials can undergo an irreversible phase transformation to another O2-type if the voltage is too high, which is a major problem for most layered TMO cathodes and will be addressed in the main work of this thesis.

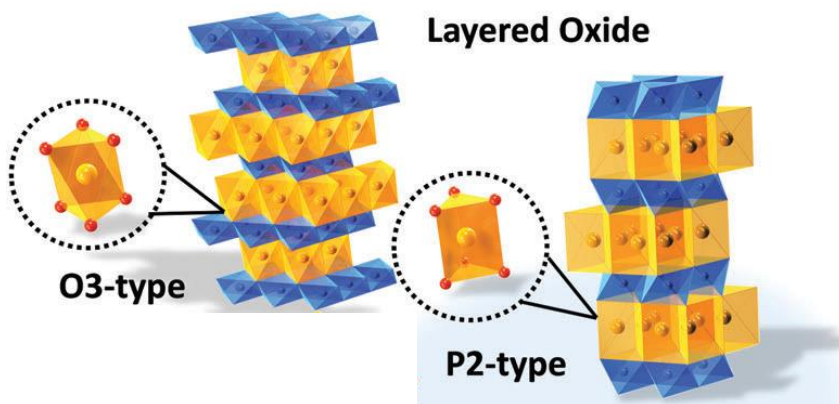


Figure 12: Illustration of O3- and P2-type layered oxide cathodes.¹⁴

The most basic form of these materials is NaMO_2 , where M is a transition metal oxide, such as $\text{Na}_{1-x}\text{FeO}_2$,⁶⁵ NaCrO_2 ,⁶⁶ $\text{Na}_{1-x}\text{MnO}_2$,⁶⁷⁻⁶⁹ $\text{Na}_{1-x}\text{CoO}_2$,⁶⁴ and $\text{Na}_{1-x}\text{NiO}_2$.⁷⁰ Most of these materials are not as stable as their lithium counterparts due to sodium's larger size and cannot accommodate one sodium per unit cell. Instead, these materials are created to be sodium deficient with $x > 0.33$

in $\text{Na}_{1-x}\text{MO}_2$. While some TMO materials like the ones mentioned above contain one type of transition metal, most of the current research in TMO cathodes use ratios of different metals, such as $\text{Na}_{0.66}(\text{Ni}_{0.33}\text{Mn}_{0.66-x}\text{Ti}_x)\text{O}_2$,⁷¹ $\text{Na}_{0.66}(\text{Ni}_{0.33}\text{Mn}_{0.66})\text{O}_2$,⁷² $\text{Na}_{0.67}(\text{Mn}_{0.65}\text{Fe}_{0.2}\text{Ni}_{0.15})\text{O}_2$,⁷³ and $\text{NaTi}_{0.5}\text{Ni}_{0.5}\text{O}_2$.⁷⁴

Major advantages of layered TMO cathodes include high capacity compared to other SIB cathodes and similarity to LIB counterparts, while disadvantages include lower working potentials and incomplete compatibility with sodium due to its large ion size.

2.4.4.2 Polyanionic Compounds

In contrast to the two-dimensional layered TMO materials in the previous section, polyanionic cathodes have three-dimensional ion diffusion pathways which increases their rate performance. They tend to have poorer capacity but increased working potential compared to layered TMO cathodes. These materials, generally containing phosphate groups, have high thermal stability due to the P-O covalent bonds in their structure.¹⁴ Polyanionic cathodes have a lower conductivity than TMO cathodes and a surface coating with a conductive material such as carbon is required for good performance.

There are many classes of polyanionic materials. The basic compound is a phosphate, NaFePO_4 , the performance of which depends on its crystal structure. Maricite NaFePO_4 cannot be used as a cathode since its structure prevents the insertion of sodium ions, while olivine NaFePO_4 exhibits a decent operating voltage of 2.8 V and 120 mA h g^{-1} of capacity.⁷⁵ This phosphate cycles between NaFePO_4 and FePO_4 as sodium is inserted and extracted, while the iron undergoes a redox reaction between $\text{Fe}^{2+}/\text{Fe}^{3+}$.

Fluorophosphates such as $\text{Na}_2\text{FePO}_4\text{F}$ take advantage of the high electronegativity of fluorine to increase the overall voltage of the cathode at a cost of decreased conductivity. As was mentioned

earlier, a coating of conductive carbon can mitigate some of this disadvantage. Pyrophosphates, of the form $\text{Na}_2\text{FeP}_2\text{O}_7$, have a higher capacity but slower ion diffusion. These types of phosphates can be combined to create $\text{Na}_4\text{M}_3(\text{PO}_4)_2\text{P}_2\text{O}_7$ which has faster sodium ion diffusion. As the name suggests, sodium super ionic conductors or NASICONs, such as $\text{Na}_3\text{V}_2(\text{PO}_4)_3$, have excellent rate performance and cyclability due to their high ion conductivity and are able to maintain 96% capacity after 200 cycles at 5 C.⁷⁶ Finally, sulfates such as NaMSO_4F benefit from increased voltage due to the sulfur and fluorine atoms compared to phosphates and have demonstrated success as an LIB cathode.⁷⁷⁻⁷⁹

2.4.5 NMC Materials

This section will describe a class of cathode materials known as NMC due to the presence of three transition metals in $\text{Li}(\text{Ni}_x\text{Mn}_y\text{Co}_z)\text{O}_2$, well-known for its potential in LIBs. This material also exists as $\text{Na}(\text{Ni}_x\text{Mn}_y\text{Co}_z)\text{O}_2$ for SIBs, and while this material is a layered transition metal oxide, it deserves its own section since it is the material upon which this thesis is focused.

Batteries need a wide operating voltage window to have high energy density. On the cathode side, this means that cathodes with a high operating voltage are much sought-after. However, side reactions with the electrolyte, phase transformations, and greater volume changes that occur at high voltages impose a limit on how high a voltage the cathode can handle during cycling. The first method of addressing the problem of cathode stability is to dope the material with other transition metals.

Many examples of multi-metal layered TMOs were given in Section 2.4.4.1 but the benefits of multi-metal TMOs were not explained. The cathode material NaMnO_2 is popular because Mn is a cheap active material for a redox reaction with Li or Na at a respectable voltage, but at high content ratios it dissolves into the battery electrolyte and severely decreases cycle life. It is

therefore beneficial to substitute a portion of Mn with another metal, preferably a metal that can also participate in a redox reaction with the voltage range of the cell so capacity is not lost. Cobalt is electrochemically active in $\text{Na}(\text{Mn}_x\text{Co}_y)\text{O}_2$ compounds and its redox reaction occurs at a higher potential, so it is often substituted into manganese oxides. It also results in structural stabilization by enabling phase transitions back to P2 from O2.⁸⁰ However, cobalt is relatively expensive and high percentages of cobalt in $\text{Na}(\text{Mn}_x\text{Co}_y)\text{O}_2$ compounds are not commercially feasible. Nickel, which is also electrochemically active, can be added instead of excess Co to help stabilize layered cathode materials. Materials with high nickel content are more difficult to synthesize since it renders the material air-unstable, so the content of nickel must also be kept low. It is understandably complicated to balance the pros and cons of each element to create an optimized cathode material. The metal ratio optimization of this thesis's material, $\text{Na}_{0.66}(\text{Ni}_{0.13}\text{Mn}_{0.54}\text{Co}_{0.13})\text{O}_2$, has previously been conducted by another group member and is not in the scope of this thesis.^{81,82}

Other metals outside of the NMC category have also proven to be beneficial for SIB cathodes. Xu et al. substituted a small amount of Li in the P2 structure of $\text{Na}_{0.66}(\text{Ni}_{0.33}\text{Mn}_{0.66})\text{O}_2$ to obtain $\text{Na}_{0.80}(\text{Li}_{0.12}\text{Ni}_{0.22}\text{Mn}_{0.66})\text{O}_2$ which exhibited no significant phase transition up to 4.4 V and maintained 91% capacity retention after 50 cycles.⁸³ Singh et al. compared $\text{Na}_{2/3}[\text{Ni}_{1/3}\text{Mn}_{2/3}]\text{O}_2$ and $\text{Na}_{0.67}[\text{Ni}_{0.2}\text{Mg}_{0.1}\text{Mn}_{0.7}]\text{O}_2$ and found that the addition of Mg suppresses the P2-O2 transition but creates a new OP4 phase above 4.2 V.⁸⁴ Capacity was somewhat reduced but capacity fading was reduced to only 6 mA h g⁻¹ after 50 cycles. Doping with Zn was also demonstrated to stabilize the P2 structure at high voltages.⁸⁵ These cation-doped materials have increased stability but their rate performance is still inadequate.

Several sodium NMC cathodes have been studied and characterized in SIBs, including $\text{Na}_{0.45}(\text{Ni}_{0.22}\text{Co}_{0.11}\text{Mn}_{0.66})\text{O}_2$, $\text{NaNi}_{0.33}\text{Mn}_{0.33}\text{Co}_{0.33}\text{O}_2$, $\text{Na}_{0.67}(\text{Mn}_{0.65}\text{Co}_{0.2}\text{Ni}_{0.15})\text{O}_2$, and $\text{Na}_{0.66}(\text{Mn}_{0.54}\text{Co}_{0.13}\text{Ni}_{0.13})\text{O}_2$.^{14,71,73,86–90} These materials have a high initial capacity but are only stable below 4.3 V. Above 4.3 V, the P2-type cathodes undergo an irreversible phase transition to O2-type which causes a large capacity loss upon cycling, and metal dissolution into the electrolyte at high voltages further decreases performance. For example, Wang et al. reported a capacity retention of 94% for $\text{Na}_{0.66}(\text{Ni}_{0.33}\text{Mn}_{0.66})\text{O}_2$ after 100 cycles between 2.0 and 4.0 V but only 29% between 2.0 and 4.5 V at the same current rate of 0.1 C.⁷²

2.5 Coating

The second method of increasing cathode stability at higher voltages is to coat the electrode with a protective layer. These surface coatings can act as a buffer for volume changes during charge/discharge and prevent particle breakdown. Coatings can also protect the electrode from harmful electrolyte interactions including side reactions and dissolution of the active material into the electrolyte. Finally, surface coatings can provide increased electrical or ionic conductivity. Surface coating with carbon has been demonstrated many times to improve stability and cycling performance of cathodes, but this creates a layer of inactive material on the surface of the cathode which reduces overall capacity and is detrimental to materials containing Co due to a side reaction.^{91–93} Instead of carbon coating, a metal oxide coating can offer the same protection against dissolution into the electrolyte while adding capacity and improving cyclability up to 4.5 V.^{81,82}

2.5.1 Atomic Layer Deposition

Atomic layer deposition (ALD) can be used to create a homogeneous defect-free ultrathin coating of metal oxides on an electrode and this strategy has been used to improve the performance

of LIBs. ALD is a method for depositing ultrathin coatings on a substrate using two gas-phase reactants that are alternatingly introduced to the sample surface separated by a purging step. Each time a gas reactant is introduced, the gas molecules form a monolayer on the sample surface and the purge removes all free gas molecules. When the next reactant is introduced, its molecules react with the molecules on the sample's surface, forming another monolayer as shown in Figure 13. Metal oxides are the most common materials deposited by ALD. In this manner, high-quality, defect-free, and homogeneous ultrathin films can be deposited on battery electrode materials.

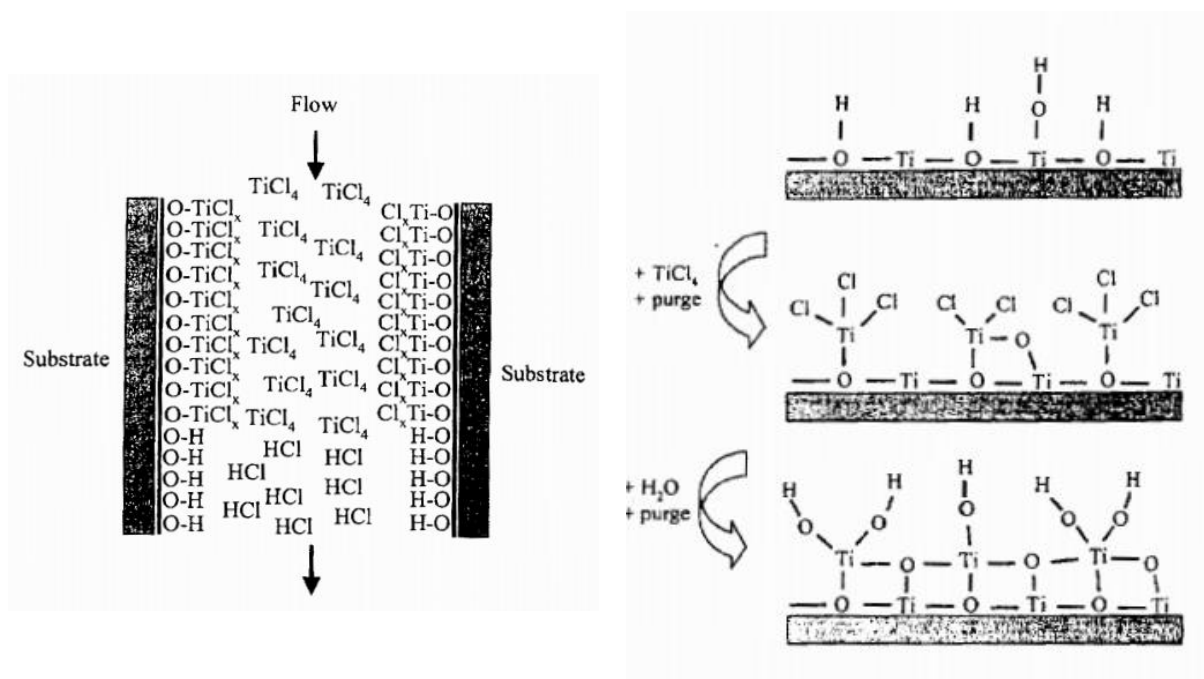


Figure 13: Schematic of ALD mechanism with TiCl₄ and H₂O as the precursors.⁹⁴

Al₂O₃, TiO₂, ZrO₂, and SnO₂ have been deposited by ALD on LIB electrodes by Xueliang Sun's group in 2014 to demonstrate improved cycling stability.⁹⁵⁻⁹⁷ They discovered that an ultrathin ALD coating of Al₂O₃ increases the LiCoO₂ cathode's cyclability the best but ZrO₂ improves rate capability better due to its higher conductivity.⁹⁵ The same group also demonstrated the addition of a layer of solid-state electrolyte on a LiNi_{1/3}Co_{1/3}Mn_{1/3}O₂ cathode by ALD to

improve high-voltage performance.^{98,99} Other examples of ALD metal oxide coatings include SnO₂ on graphene and TiN on Li₄Ti₅O₁₂.^{100,101} The application of ALD coating to SIB electrodes has only recently garnered some attention but the field is still very underdeveloped. The first example of ALD deposition was on a tin anode for SIBs was reported by Han *et al.* in 2013.¹⁰² Their work exhibited the ability of ALD-deposited Al₂O₃ to significantly stabilize tin nanoparticles during the large volume changes occurring throughout charge and discharge cycling. Later, Kaliyappan *et al.* reported coating alumina on Na_{2/3}(Mn_{0.54}Ni_{0.13}Co_{0.13})O₂ for a more stable SIB cathode and continued their investigation by coating ZrO₂ and TiO₂ as well.^{81,82}

Similar to ALD, molecular layer deposition (MLD) can deposit ultrathin coatings composed of small molecules while retaining precise control on coating thickness and conformity.^{103,104} MLD can create ultrathin polymer films or polymer-metal films and has been used to increase the mechanical stability and combat the huge volume expansion of a Si anode.¹⁰⁵ One type of polymer-metal coating, called metalcone, consists of metal oxides and short organic molecules and has gained some attention for battery applications.^{103–108} An alucone coating, made by alternating reactions between trimethylaluminum and short organic diols such as ethylene glycol or glycerol as depicted in Figure 14, has been shown to be effective at preventing the shuttle effect caused by the dissolution of polysulfides in Li-S batteries.^{107,109} Other groups have studied the effect of alucone on silicon electrodes for LIBs and have similarly verified alucone's ability to protect electrodes and improve their cycle life.^{106,108} Alucone has distinct advantages over alumina in that it is a) less dense allowing for better ion diffusion, b) more flexible and soft improving its stabilizing effect on high-volume-change materials, and c) more conductive than alumina due to its carbon linkers.^{103,104} Alucone has a density of 1.5 g/cm³ while alumina is twice as dense at 3.0 g/cm³, and alucone's hardness is only 1 GPa compared to alumina's 13 GPa.¹⁰³ This thesis

demonstrates that these qualities of alucone do indeed increase the capacity, rate performance, and cycle life of NaNMC cathodes for SIBs.

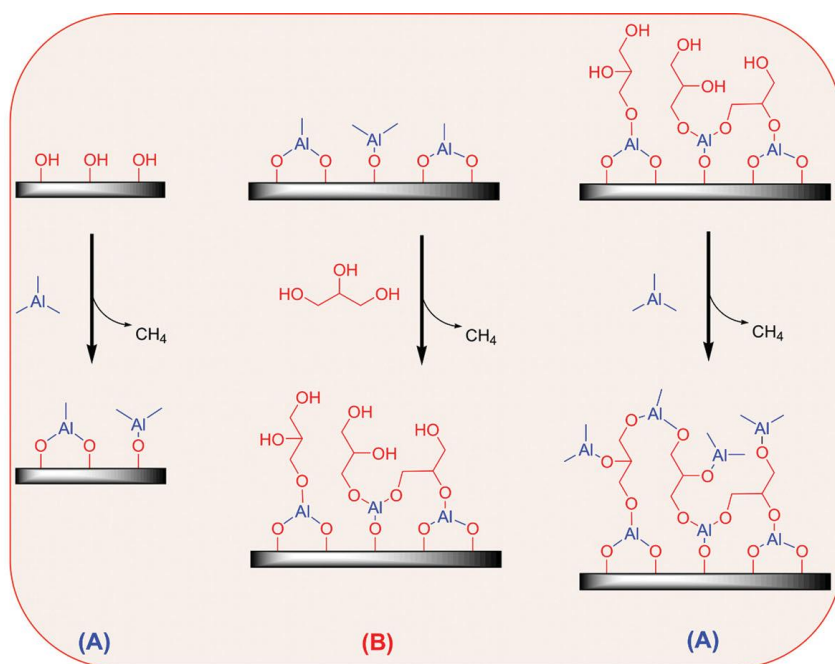


Figure 14: Reaction mechanism of MLD of alucone using trimethylaluminum and glycerol.¹⁰⁵

3 Characterization Methods

3.1 X-Ray Diffraction (XRD)

XRD is a quick and versatile way to determine a sample's crystal structure and composition by comparing its spectrum with known spectra. When photons of a certain wavelength interact with the evenly-spaced planes in a crystal, the photons can diffract and interfere constructively resulting in a more intense signal which can be detected. The condition for this constructive interference is given in Equation 5 below known as Bragg's Law:

$$n\lambda = 2d \sin\theta \quad (5)$$

where n is an integer, λ is the wavelength of the incident photon, d is the interlayer spacing of the crystal, and θ is the angle of the incident photon. This phenomenon is illustrated in Figure 15. When this condition is not met the photons will interfere destructively and detection of the diffracted photons, caused by the interactions between the photon and electrons in an atom's orbital, will be suppressed.

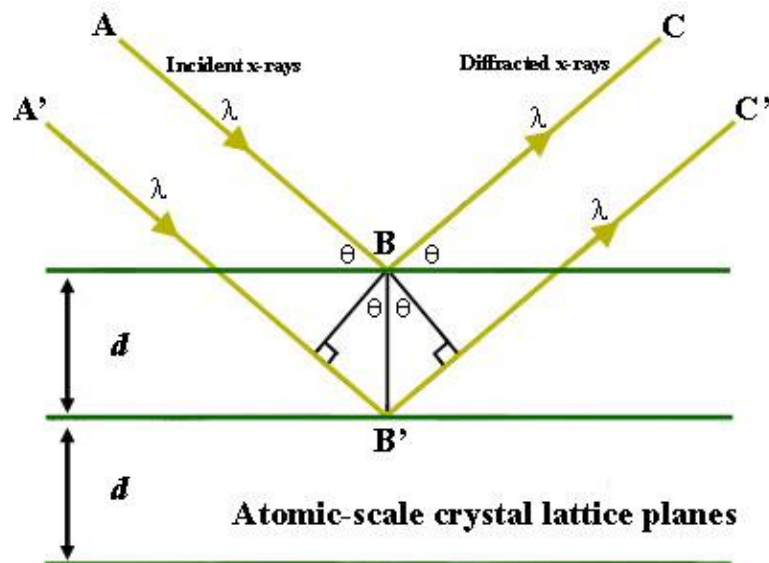


Figure 15: Bragg's diffraction of X-rays in crystal lattice planes.¹¹⁰

A typical XRD instrument consists of an X-ray source, a rotating sample holder, and a detector. X-rays are ideal for Bragg's Law diffraction since their wavelengths are on the order of crystal lattice interlayer spacing. X-rays can be generated by striking a copper plate with an electron beam and directed using a collimator to guide them onto the sample. The stage holding the sample can rotate to change the incident angle of the X-rays or the X-ray source can rotate. Diffracted X-rays hit a detector which measures intensity which can be plotted against 2θ and compared to literature reports or theoretical calculations to confirm sample structure and composition. The peak broadening can also be used to measure the crystallite size.

In this work, XRD is the main characterization method for confirming the successful synthesis of NaNMC and verifying its structure.

3.2 Scanning Electron Microscopy (SEM)

SEM is a common method for characterizing a sample's surface morphology, size, shape, and even composition. While SEM can be used on many types of materials across many disciplines, the main limitation is that the sample's surface must be conductive. Non-conductive samples can still be imaged if a thin layer of a conductive material, such as gold, is first coated onto the sample. This coating does not usually interfere with SEM characterization, although its presence can be detected during energy dispersive X-ray spectroscopy and might be seen at high magnification. SEM instruments typically have a resolution between 1-10 nm.

SEM instruments have several key operating components, shown in Figure 16. First, electrons are generated by passing a current through a tungsten filament which produces a very high electric field at its tip, pulling electrons out. These electrons are accelerated in an applied electric field and directed through a column using condenser lenses and deflection coils. The entire system must be

kept under vacuum to avoid airborne particles deflecting the electron beam. This limits SEM use for characterizing biological samples since they can become damaged under high vacuum. The final condensed beam is swept back and forth across a sample in a raster scan and various detectors measure the scattered electrons and photons.

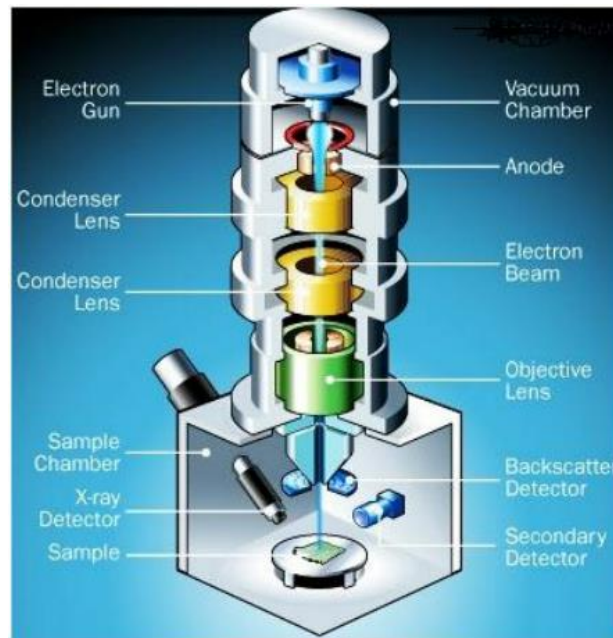


Figure 16: Components of a SEM.¹¹¹

Some of the incident electrons hit atomic nuclei in the sample are backscattered directly. These electrons carry some information about the sample composition, since the number of backscattered electrons is directly proportional to the atomic mass of the sample's atoms. Heavier elements will appear brighter in SEM images than lighter elements. Secondary electrons are emitted from the sample's surface when the incident electrons interact with a sample atom's electron and these are detected to give topographical information about the sample's surface. If a secondary electron is generated from an inner electron orbital, an outer electron can drop down to the vacant lower energy state and release its energy in the form of an X-ray photon. These X-ray photons can be

detected to give information about the sample's composition since the energy of these photons is characteristic of the atom from which it came.

In this work, SEM is only used for particle morphology characterization since its resolution is too low to see the MLD layers and other techniques such as XRD and ICP are more accurate for confirming composition.

3.3 Transmission Electron Microscopy (TEM)

TEM is useful for imaging samples at the nanoscale and sub-nanoscale. TEM is similar to SEM in that both techniques generate an electron beam and direct it at a sample, but TEM detects the electrons that transmit through the sample instead of those that scatter back from the sample's surface. Electrons that pass through a sample are captured by a fluorescent screen. TEM instruments operate at a much higher accelerating voltage than SEM (up to 300 kV compared to 40 kV), meaning that the electrons have a shorter wavelength and resolution is improved. Crystal structures, lattice dimensions, and even atoms can be viewed using TEM, making it a powerful characterization tool.

One limitation for using TEM is that samples must be extremely thin or the incident electrons will all be absorbed by the sample and none will reach the detector on the other side. Since ALD and MLD are surface coating techniques and the edges of a material are generally much thinner than the middle sections, TEM is ideal for measuring the coating thickness and viewing coating homogeneity. As with SEM, TEM must be performed under high vacuum, so some biological samples may become damaged during imaging.

This work uses TEM to confirm the presence of a coating layer after using MLD to deposit alucone on electrodes. The thickness of this coating layer is also measured using TEM to confirm that the deposited thickness per MLD cycle matches that reported by other researchers.

3.4 Thermogravimetric Analysis (TGA)

TGA uses a very precise balance to measure the weight change of a sample as temperature is slowly increased under gases such as air or argon. This can give clues about the composition of the sample since different molecules decompose at different temperatures. The weight loss as temperature is increased in the presence of various gases can also indicate at what temperatures reactions take place. This was used to determine what annealing temperature was required for optimum synthesis of NaNMC since at lower temperatures the reaction is not complete and at higher temperatures other phases can form.

3.5 Inductively Coupled Plasma Atomic Emission Spectroscopy (ICP-AES)

ICP-AES is an analytical technique for determining elemental composition. Samples for ICP-AES measurements must first be digested in an acid which is introduced to the ICP instrument and turned into a mist by a nebulizer. Argon gas is ionized in the instrument to create a high-temperature plasma into which the sample mist is injected. The sample's molecules break up into atoms which are ionized and deionized continually which causes a characteristic wavelength to be emitted from the atom's electrons as they fall from an excited state to a ground state. The intensity and wavelength of the emitted light is used to accurately determine the sample's elemental composition. ICP-AES was used in this work to confirm successful synthesis of the NaNMC sample by measuring its composition. One limitation of this analytical technique is that it cannot

accurately determine the oxygen content in a sample due to the presence of oxygen in the digestion liquid and the atmosphere.

3.6 Battery Cycling

The most important characterization tool for battery materials is electrochemical cycling of the material assembled in a cell. Galvanostatic cycling of a half-cell assembly is the most common method of testing a battery material's performance. Galvanostatic cycling involves measuring the voltage response of a battery under a constant current. As a cell is charged under a constant current, ions and electrons move from the cathode side to the anode side until the voltage drops below a certain threshold. Upon discharge, the reverse happens, and the capacity of the cell can be determined, as well as the shape of the charge/discharge profile which is indicative of the electrochemical processes in the cell.

Testing electrode performance in a half-cell, where one electrode is pure sodium, isolates the behaviour of the electrode of interest. To assemble a half-cell, a cathode is placed in a cathode casing, followed by a disk of glass fibre, a Celgard separator, and another glass fibre disk. The glass fibre disks serve as reservoirs for the electrolyte and the separator prevents contact between the two electrodes which would result in a short-circuit. The anode is added next, followed by a steel spacer, a spring, and the anode casing which has a rubber gasket to seal the cell. Cell assembly is performed in an argon-filled glovebox since the electrolyte and sodium react with the oxygen and water in air. Cell cycling was performed on a Lanhe Battery Testing System at various current rates and voltage ranges.

3.7 Electrochemical Impedance Spectroscopy (EIS)

EIS is a measurement of a material's ionic/electrical resistance as a function of frequency. An alternating voltage at different frequencies is applied to an assembled cell and the response is measured. The results are commonly displayed in a Nyquist plot as shown in Figure 17, with the imaginary impedance Z'' (Ω) on the y-axis and the real impedance Z' (Ω) on the x-axis. From this plot, important information about the electrochemical processes inside the cell can be obtained. The x-intercept at the left of the plot is the resistance of the whole system while the semicircle seen on a Nyquist plot represent the resistance from the electrode materials and the electrode-electrolyte interface. A smaller semicircle means there is less resistance for charge transfer which is critical for better battery performance. The 45° tail on the right of the plot known as the Warburg diffusion regime represents resistance caused by diffusion limits and particle size. A larger particle will have a higher resistance since it takes longer for ions and electrons to diffuse between the inner and outer portions of the particle.

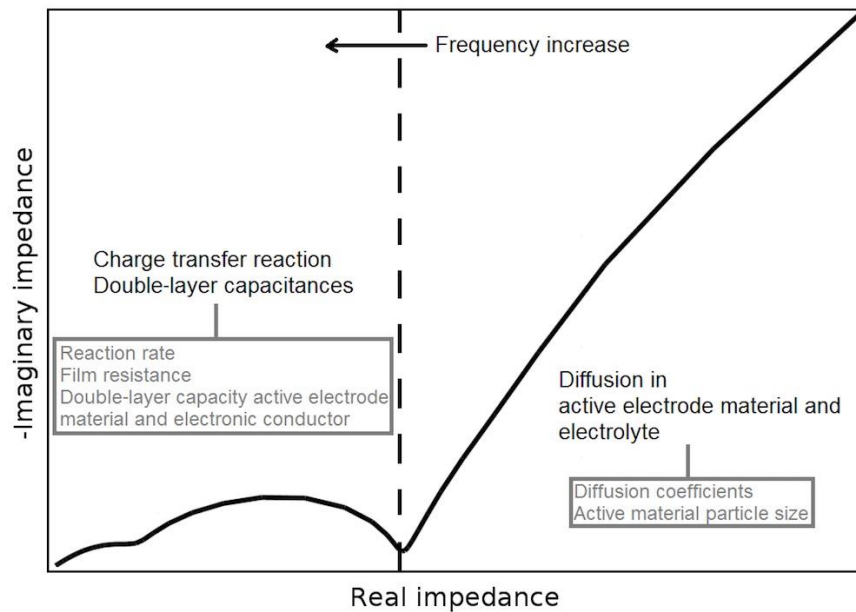


Figure 17: Nyquist plot of a typical EIS measurement on a half-cell battery assembly.¹¹²

This work aims to use EIS to demonstrate that an alucone coating by MLD reduces resistance in the charge transfer reaction between the electrolyte and the NaNMC cathode. Since MLD does not significantly change the size of a particle the tail in the Warburg diffusion region is not helpful for characterization, but the size of the semicircle will provide information on the interface resistance. Additionally, EIS measurements before and after cell cycling can give information on a material's stability since an increase in size of the impedance semicircle after cycling is evidence of destructive instability.

4 Synthesis and Characterization of NaNMC

This section will describe the optimization of the synthesis of $\text{Na}_{0.66}(\text{Ni}_{0.13}\text{Mn}_{0.54}\text{Co}_{0.13})\text{O}_2$, referred to hereafter as NaNMC. Temperature and chelating agent optimization will first be presented followed by physical characterization of the finalized material.

A sol-gel method was used to synthesize NaNMC microflakes. Appropriate amounts of Na, Ni, Mn, and Co acetates (0.271, 0.162, 0.662, and 0.162 g, respectively) were dissolved in 50 mL of distilled deionized water. 30 mmol of a chelating agent was added and the mixture was stirred at a temperature of 110 °C for five hours, then at 50 °C overnight until a viscous solution remained. This product was placed in a muffle furnace under air for 4 h at 400 °C, ground, then transferred to a tube furnace and annealed at 800, 850, or 900 °C for 12 h in air. The product was ground and used for physical characterization, then mixed with additives for electrode fabrication which will be described later.

4.1 Temperature Optimization

The first step in optimizing the synthesis of NaNMC microflakes was determining the effect of temperature during the annealing phase. For an idea of what temperature is needed for complete reaction of the acetates, TGA was first performed on the viscous solution of the acetates, the result of which is shown in Figure 18. The decrease in weight seen in Section I up to 100 °C is attributed to the evaporation of residual water. The weight loss in Section II can be attributed to the decomposition of acetates into oxides while the slower loss after 200 °C in Section III is likely due to the more complex decomposition of organic compounds or crystallization of the NMC phase.¹¹³ After 800 °C the weight of the sample remains constant, indicating that the reaction is complete.

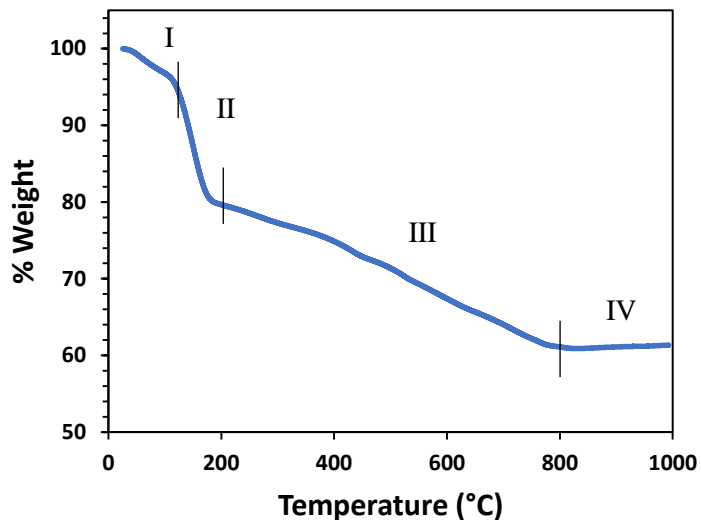


Figure 18: TGA of the viscous metal acetate solution.

After determining from TGA that the reaction appears to end around 800 °C, it was decided to test annealing temperatures of 800, 850, and 900 °C. XRD spectra of samples annealed at these temperatures are shown in Figure 19. The bottom two traces, for 800 and 850 °C, closely match established literature values for peak locations of sodium NMC materials. However, the spectrum of the sample annealed at 900 °C shows some extra peaks indicating the presence of an impurity. The asterisks denote these extra peaks which may also belong to a different phase. It was concluded that 900 °C was too high of an annealing temperature since it resulted in impurity peaks in the XRD spectrum. Any difference between annealing temperatures of 800 and 850 °C was not observable by XRD.

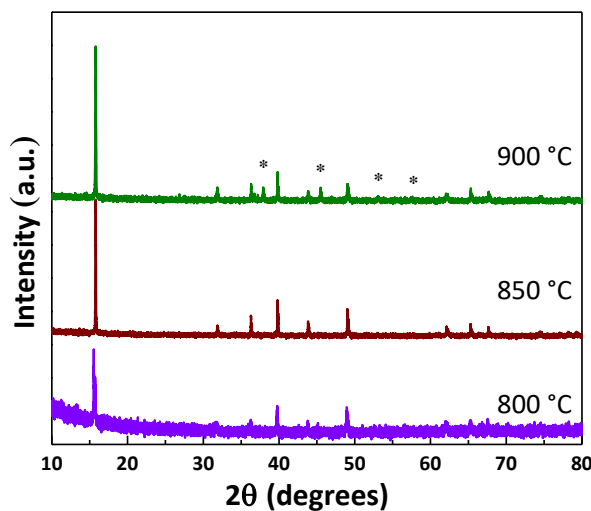


Figure 19: XRD spectra of NaNMC annealed at 800, 850, or 900 °C. The asterisks (*) denote extra peaks possibly belonging to NaMn_2O_4 .

Electrochemical testing was also performed on these annealed samples to see if their performance changed based on the annealing temperature. Figure 20 displays the capacity at 1 C and rate performance at multiple currents rates for each of these samples. The sample annealed at 850 °C had the best capacity with an initial capacity of 120 mA h g^{-1} , while the 900 °C sample had the worst capacity, starting at 90 mA h g^{-1} . All samples showed similar capacity fading after 30 cycles. The 850 °C sample also had the best rate performance shown in Figure 20b and again the 900 °C sample performed the worst. These results were supported by the XRD results since an annealing temperature of 900 °C contains impurities that likely affected the battery's performance. While an annealing temperature of 800 °C seemed to cause a complete reaction as shown in the TGA results, these electrochemical tests suggest that perhaps the crystallinity is poor and a slightly higher temperature of 850 °C results in a more homogenous crystal structure. Thus it can be concluded that 850 °C is an appropriate temperature for annealing the NaNMC precursors.

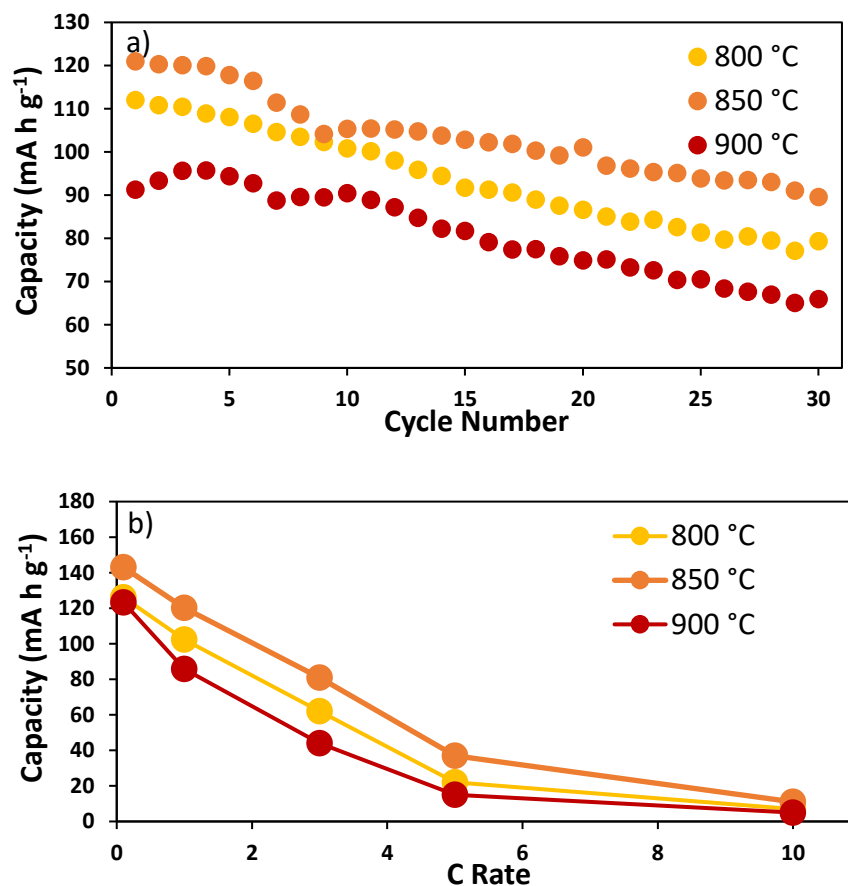


Figure 20: a) Capacity at 1 C and b) rate performance of NaNMC annealed at three different temperatures.

4.2 Chelating Agent Optimization

Reactions involving metals in water sometimes include a chelating agent. Chelation refers to the formation of a coordinate bond between metal ions and other molecules and such molecules can stabilize the metal ions in water which facilitates other reactions. Adding a chelating agent can also prevent particle agglomeration which is important in battery applications to increase surface area and diffusion of sodium ions between the electrolyte and the centre of particles. Many organic compounds, including acids, can act as chelating agents. To determine the effect of adding a chelating agent to the sol-gel synthesis of NaNMC, 30 mmol of four chelating agents were added to different batches: citric acid (CA), adipic acid (AA), ascorbic acid (AsA), and glycolic acid

(GA). The XRD of each sample synthesized with chelating agents is shown in Figure 21 and it is clear that the addition of these agents does not affect the structure of NaNMC since neither peak position or relative intensity change.

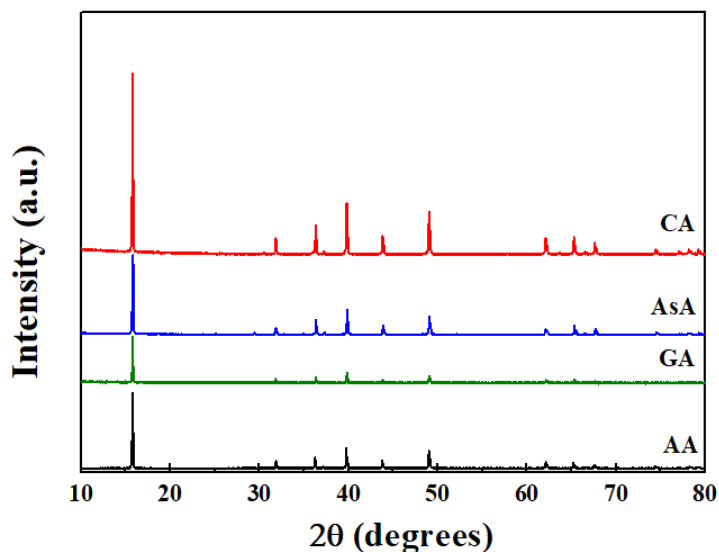


Figure 21: XRD spectra of NaNMC samples synthesized with various chelating agents: citric acid (CA), ascorbic acid (AsA), glycolic acid (GA), and adipic acid (AA).

After annealing and incorporating the powders into a coin cell assembly, their electrochemical performance was evaluated. The rate performance and cycle life from 2-4.3 V of each material are displayed in Figure 22. The rate performance, capacity, and cycle life for the citric-acid-assisted sol-gel synthesis is superior to that of all other chelating agents while the glycolic acid and adipic acid perform the worst. Although it is not understood why this chelating agent performs better, it was chosen for the synthesis of the final product due to the increase in performance compared to other chelating agents.

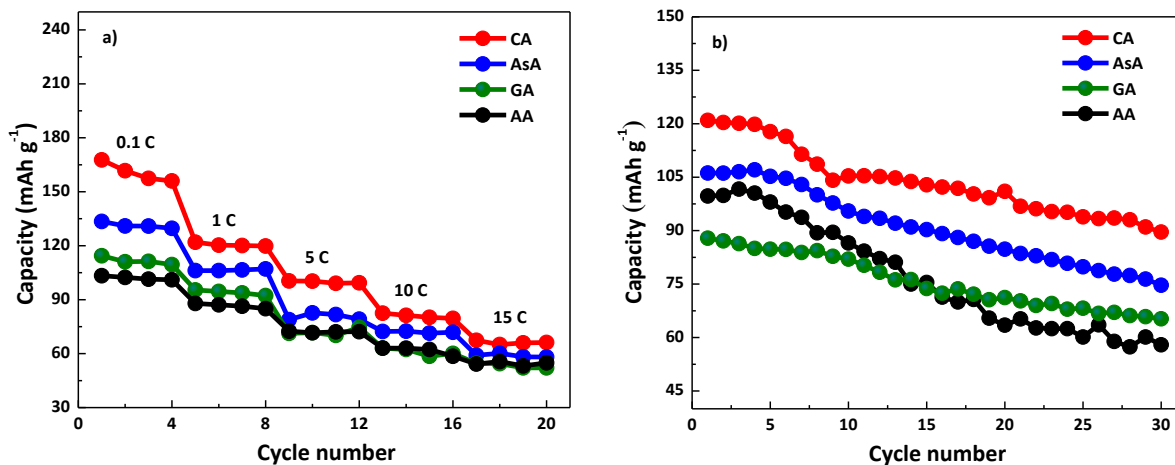


Figure 22: a) Rate performance from 2-4.3 V and b) cycle life from 2-4.3 V at 0.5 C of NaNMC synthesized with various chelating agents.

4.2.1 Synthesis and Characterization of Final Composition

The synthesis of the final NaNMC material was performed as described at the beginning of Section 4 assisted by citric acid as the chelating agent and annealed at a final temperature of 850 °C in accordance with the research that supported these conditions.

An XRD spectrum shown in Figure 23 was first taken to confirm that the synthesized material conformed to the expected crystal structure. The spectrum clearly matches the PDF card for sodium NMC materials and contains no extra peaks indicating the presence of impurities.

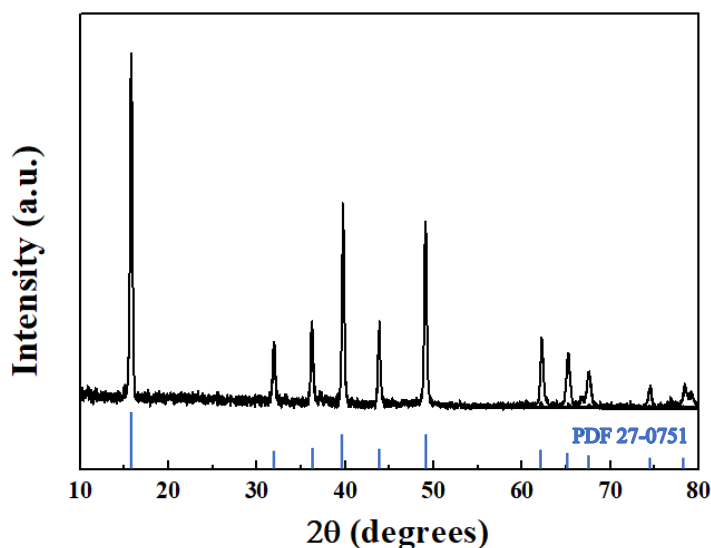


Figure 23: XRD of as-synthesized NaNMC compared to PDF No:27-0751.

The ratio of the metallic elements of the as-synthesized NaNMC was established using ICP-AES and is displayed below in Table 2. The expected ratio of each element is compared to the results returned from the ICP measurement and the Ni, Mn, and Co compositions are very close to their expected values, indicating that the synthesis was successful. The Na content deviates slightly from the expected ratio by 11%, but Na content matters the least since it can be replenished during charging. Note that ICP-AES is not able to accurately determine oxygen content since there is too much background noise from oxygen in the testing chamber and the solvent.

Table 2: Elemental composition of NaNMC from ICP-AES

Element	Expected Ratio	Actual Ratio
Na	0.66	0.593
Ni	0.13	0.127
Mn	0.54	0.527
Co	0.13	0.125

The next step was to determine the particle morphology and SEM was used to accomplish this. Figure 24 shows that the particles are microflakes with diameters of around 2 μm and thicknesses of 200 nm. It is important to note that the performance of this material could likely be improved if the particle shape was optimized to be thinner to reduce diffusion resistance for ions reaching the center of each flake, but shape optimization is not in the scope of this thesis. Further, it is speculated that the performance improvement would not be that great since the microflakes are fairly thin to begin with.

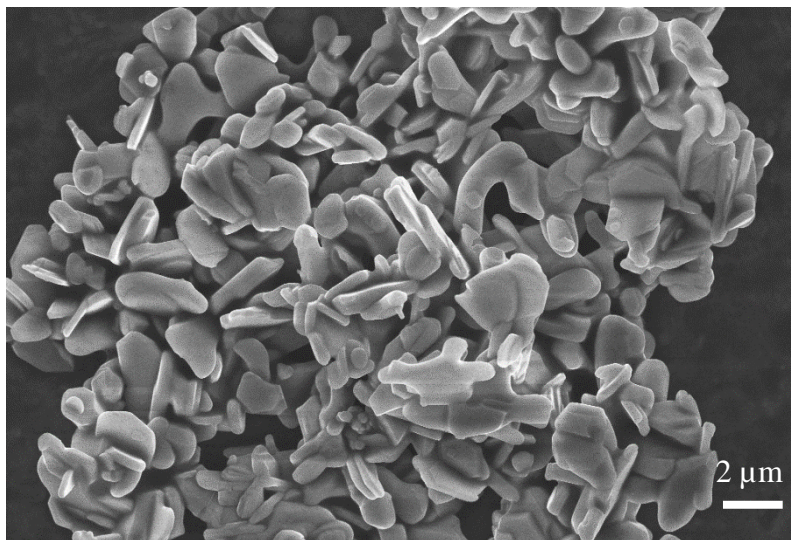


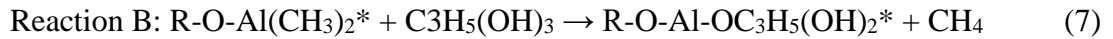
Figure 24: SEM image of as-synthesized NaNMC microflakes.

The XRD, ICP, and SEM data indicate that the synthesized NaNMC microflakes have the expected crystal structure, elemental composition, and particle morphology. Once this was confirmed, the NaNMC could be coated using MLD.

5 MLD Coating and Results

5.1 MLD Coating and Characterization

The molecular layer deposition of alucone on the NaNMC microflakes was accomplished using a Thermal Gemstar 6XT (Arradiance, LLC, USA) instrument. The precursors used were trimethylaluminum, $\text{Al}(\text{CH}_3)_3$, and glycerol, $\text{C}_3\text{H}_5(\text{OH})_3$, which reacted according to the following formula in which the asterisks denote surface species and the R represents the underlying NaNMC:



These two reactions constitute one MLD cycle, as depicted again in Figure 25, and was repeated as many times as necessary to obtain the desired coating thickness. The pulse time for both precursors was 20 ms, the deposition temperature was 115 °C, and the purge gas was nitrogen. This work compares MLD coatings of 5, 10, and 20 cycles and uses a 50-cycle coating for TEM viewing. Since both the trimethylaluminum and glycerol have multiple bonding sites, crosslinking can occur in the MLD layers which strengthens the coating layer while maintaining a porous structure to allow for faster ion diffusion. The network of aluminum, oxygen, and carbon ligands is called alucone and the by-product is methane.

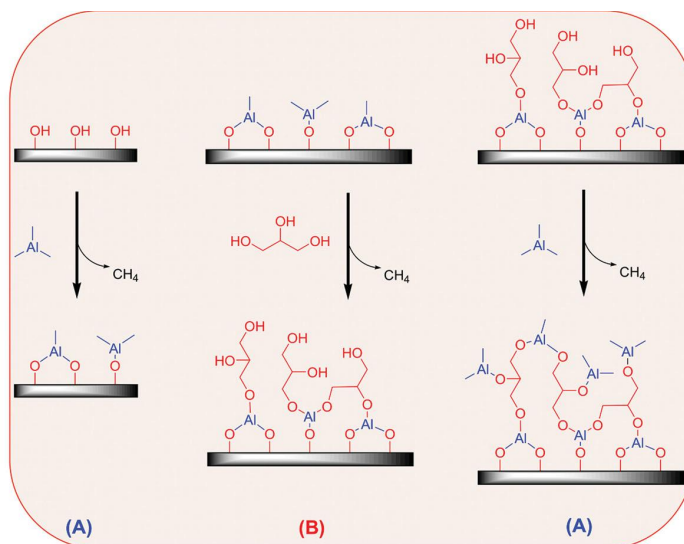


Figure 25: Reaction mechanism of MLD of alucone using trimethylaluminum and glycerol.¹⁰⁵

Each AB cycle is known to produce a coating of approximately 1.5 Å at deposition temperatures between 110 and 150 °C according to a number of studies.^{103,105,107,114} TEM was performed on an NaNMC sample that had been coated with 50 MLD cycles to determine the coating thickness per cycle. Using fewer cycles would lead to inaccuracy in this measurement which is why 50 cycles were coated. The TEM image of this sample is shown in Figure 26. The light-coloured alucone layer has a thickness of 6.3 nm corresponding to a cycle thickness of 1.3 Å which is in accordance with the aforementioned literature values.

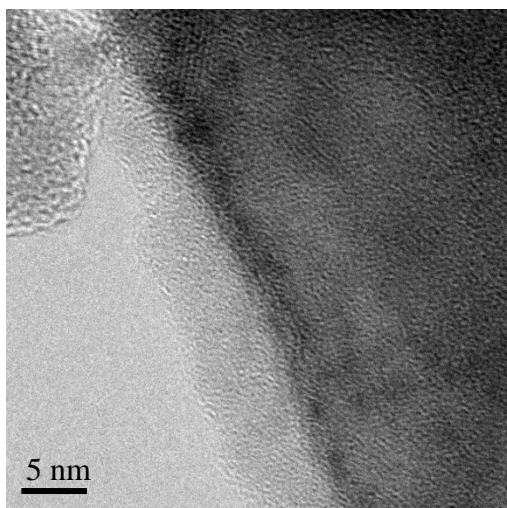


Figure 26: TEM image of NaNMC (dark) with 50 cycles of alucone coating by MLD.

5.2 Electrochemical Characterization

Cathodes for electrochemical characterization were individually created by grinding uncoated NaNMC with Ketjenblack carbon for conductivity and a 10:1 mixture of acetylene black and Teflon as binder, in a total ratio of 70:20:10. These powders were ground with ethanol to create a paste, pressed into a steel mesh current collector, and dried overnight at 80 °C. These cathodes were then coated with alucone by 5, 10, or 20 cycles of MLD since it has been demonstrated that coating the fabricated cathode results in better performance than coating the plain active material powder first.⁸² The coated cathodes were assembled into coin cells with sodium as the anode according to the method described in Section 3.5. A solution of 1 M NaClO₄ in a 1:1 mixture of ethylene carbonate (EC) and diethylene carbonate (DEC) with 2% fluoroethylene carbonate (FEC) as a high-voltage stabilizer was used as electrolyte.

Before discussing the electrochemical performance for the coated samples it is appropriate to demonstrate why this coating is necessary. As was mentioned earlier, NMC materials which have a P2-type crystal structure often suffer from a phase change to O2-type at high voltages, limiting their applications to below 4.3 V. To demonstrate this poor performance at higher voltages, uncoated NaNMC electrodes were cycled at 1 C to 4.3, 4.4, or 4.5 V (Figure 27). As expected, a higher voltage results in a higher initial capacity since more sodium ions can be drawn out of the cathode. However, the capacity at high voltages soon drops below that of the cell cycled at both lower voltage limits, demonstrating NaNMC's instability at high voltages. The capacity retentions for the cells cycled to 4.3, 4.4, and 4.5 V are 74, 62, and 49% respectively. The cell cycled to 4.3 V shows good stability up to 100 cycles while the cells cycled to 4.4 and 4.5 V lose capacity quickly, explaining why it is beneficial to coat NaNMCs with a protective layer.

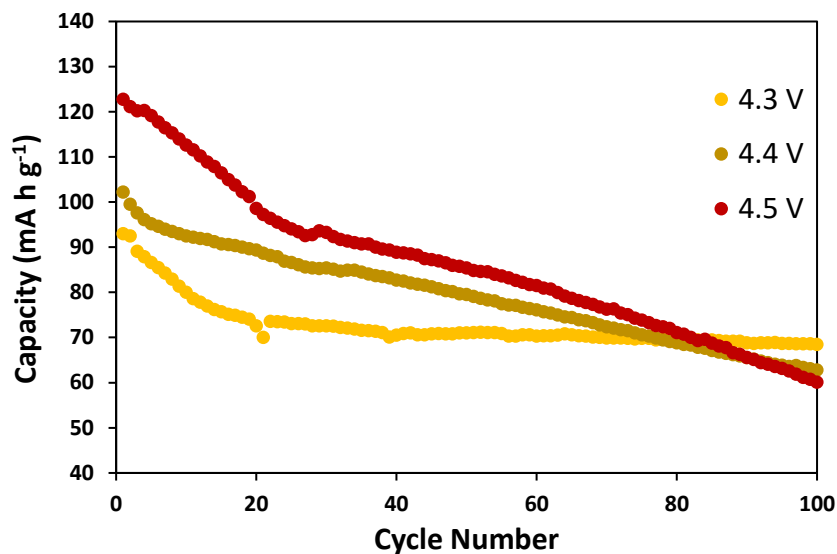


Figure 27: Uncoated NaNMC cycled at 1 C from 2 V to 4.3, 4.4, or 4.5 V.

The cycle performance of alucone-coated NaNMC at 0.5 C is shown in Figure 28. In this figure, all of the electrodes have similar capacities during the first few cycles but then differences occur. The sample with 20 layers of alucone has a capacity retention of only 56% after 100 cycles, which is very close to the uncoated capacity retention of 53%. The sample with 10 layers of alucone also has a similar capacity retention, but the sample with 5 layers outperforms the other electrodes with a capacity retention of 67% after 100 cycles. This demonstrates that the ultrathin layer of alucone is able to increase the stability of the electrode, likely because of its prevention of reactions with the electrolyte and containment during volume changes as discussed previously. The poor performance of the 20-layer sample indicates that some sort of tradeoff exists between the positive and negative effects of an alucone layer. An alucone coating 20 layers thick likely decreases ion diffusion to the point where the benefits of structural stability are negated by slower reaction kinetics. 10 layers of alucone seems to be in the middle while 5 layers is thin enough to not affect ion diffusion much. These results demonstrate the importance of control over film thickness and using MLD to deposit films on battery electrodes since other methods of coating either cannot coat ultrathin films or do not have adequate control over uniform thickness.

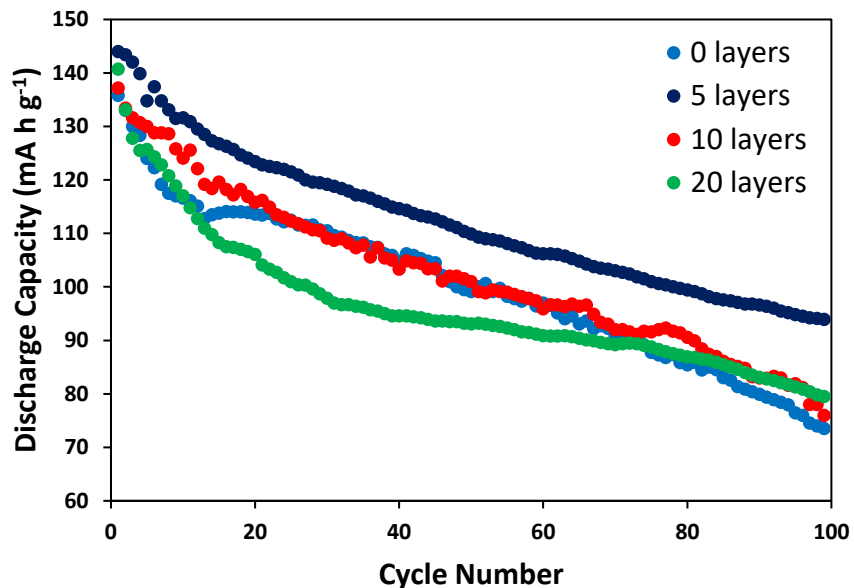


Figure 28: Cycle performance of NaNMC with 0, 5, 10, or 20 layers of alucone deposited by MLD. Cells were cycled at 0.5 C from 2-4.5 V.

The voltage profiles for the first cycles of the above graph are plotted below in Figure 29. The voltage profiles are similar for all samples but the plateaus are more defined for the coated samples. The coated samples, particularly 5-layer sample, have higher capacities than the uncoated sample as was already demonstrated in Figure 28. The voltage plateaus occur around 2.5, 3.6, and 4.2 V, which is in accordance with other sodium NMC materials reported elsewhere.^{86,89} The complex intercalation/deintercalation mechanism of NMC-type materials can be attributed to the multiple transition metal ions in the P2-type structure.

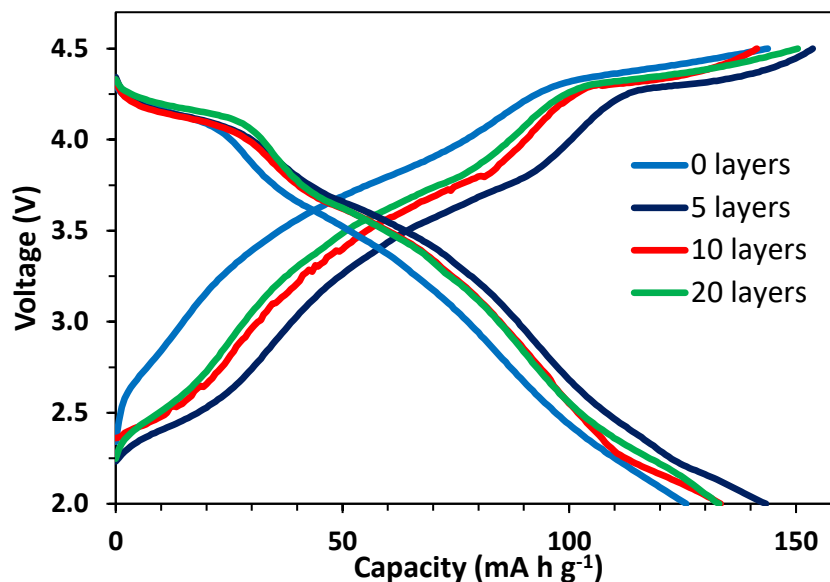


Figure 29: Voltage profiles for the first cycles of NaNMC coated with 0, 5, 10, or 20 layers of alucone at a current of 0.5 C.

The effect of the alucone coating is even more pronounced at high charge/discharge rates, show in Figure 30. At 0.5 C, all samples show similar capacities. As the current is increased from 0.5 to 1, 2, 5, and 10 C, the difference between the uncoated NaNMC and the coated NaNMC becomes more pronounced. As soon as the current is increased to 1 C, the capacity of pristine NaNMC drops about 30 mA h g⁻¹ while the coated samples drop between 10 and 20 mA h g⁻¹. At a moderate discharge rate of 5 C, the uncoated sample has a capacity half that of the coated samples and no capacity at 10 C. On the other hand, the sample with 5 layers of alucone has a higher capacity than all other samples at rates of 2, 5, and 10 C. This experiment demonstrates again that there exists an optimal coating thickness close to 5 layers since the sample with this amount of alucone outperforms the samples with no coating, 10 layers, and 20 layers of alucone.

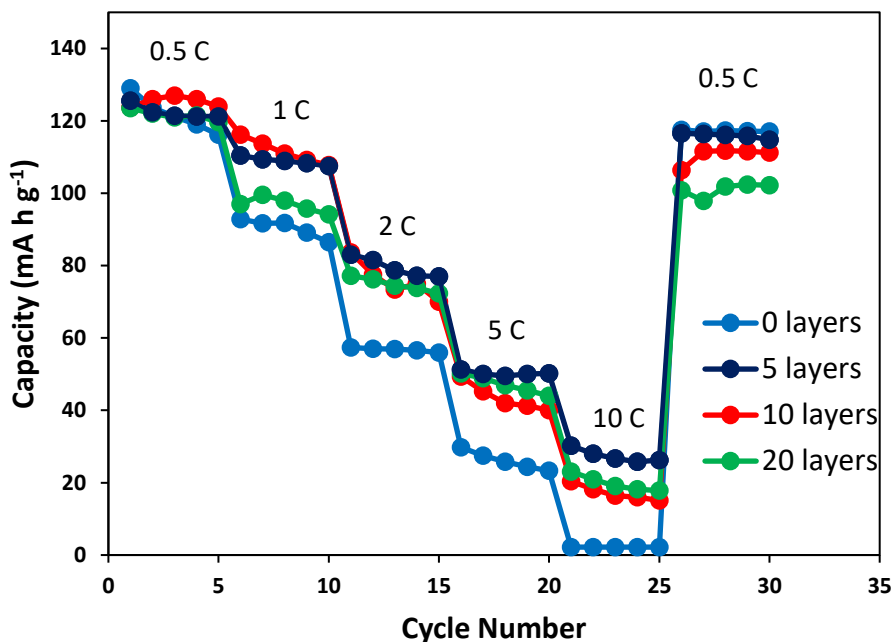


Figure 30: Rate performance of NaNMC coated with alucone. Voltage range for all samples was 2-4.5 V.

The EIS results of the assembled cells, both before cycling and after 100 cycles, are shown in Figure 31. Recall that for interpretation of EIS, a smaller semicircle indicates less film resistance which increases the rate performance. In Figure 31a, the 5-layer sample has the smallest semicircle but the uncoated sample has only a slightly higher internal resistance. The samples coated with 10 and 20 layers of alucone have higher internal resistances as evidenced by their Warburg regimes beginning at 400 and 650 Ω , respectively. It is remarkable that such a large change in the internal resistance occurs between the 5-, 10-, and 20-layer coatings. Figure 31b shows the same cells but after 100 cycles on the battery tester which can be used to draw conclusions about the cells' stability. An absence of change in the internal resistance before and after 100 cycles indicates good stability of the electrode materials while an increased resistance after 100 cycles shows that something changed in the cell to increase the resistance. In Figure 31b, the Warburg diffusion regime does not shift for the 5-layer sample, demonstrating high stability of the interface between

the electrode material and the electrolyte caused by the alucone layer. The 10-layer sample's Warburg regime shifted from 400 Ω to 580 Ω , which is an increase of 45%, while semicircle of the 20-layer sample stayed constant after 100 cycles. The largest change was observed in the resistance of the uncoated sample which increased by 150% of its uncycled value. This indicates that the uncoated sample's interface is the least stable out of all the samples, followed by the 10-layer sample, and the 5-layer and 20-layer samples has very good interfacial stability.

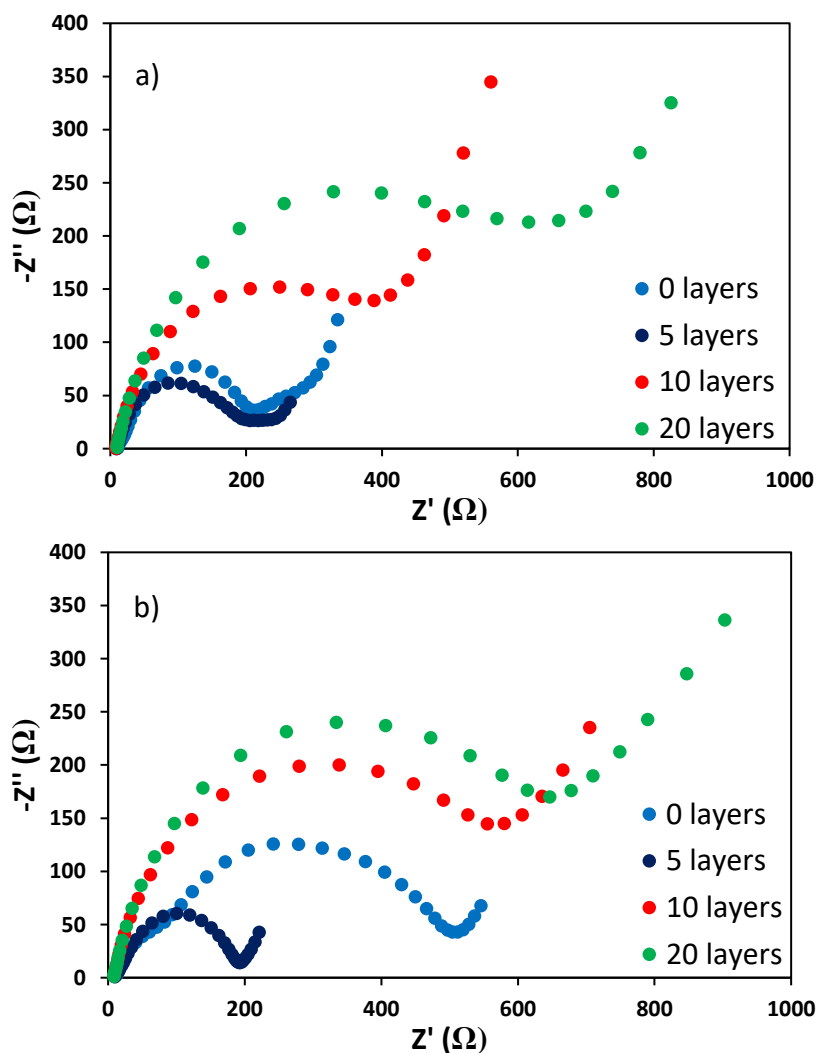


Figure 31: EIS of NaNMC coated with different layers of alucone a) before charge/discharge cycling and b) after 100 cycles at 0.5 C from 2-4.5 V in a typical coin cell setup.

Since the 5-layer sample demonstrated its ability to increase cycling stability at elevated voltages, it was appropriate to test its cycling performance at even higher voltages. The 5-layer sample was cycled between 2 V and 4.50, 4.55, 4.60, or 4.65 V at a current rate of 1 C and the results are shown in Figure 32. As was expected, greater capacity fading was observed at higher voltages since structural changes, volume changes, and electrolyte reactions are more severe at higher voltages. The cells cycled up to 4.60 and 4.65 V lost nearly all capacity at 300 cycles while the cells cycled to 4.50 and 4.55 V had capacities of 36 and 26 mA h g⁻¹ respectively. The performance of these cells cycled past 4.5 V is reasonable but the gain in energy density would not justify the decrease in cycle life in commercial applications.

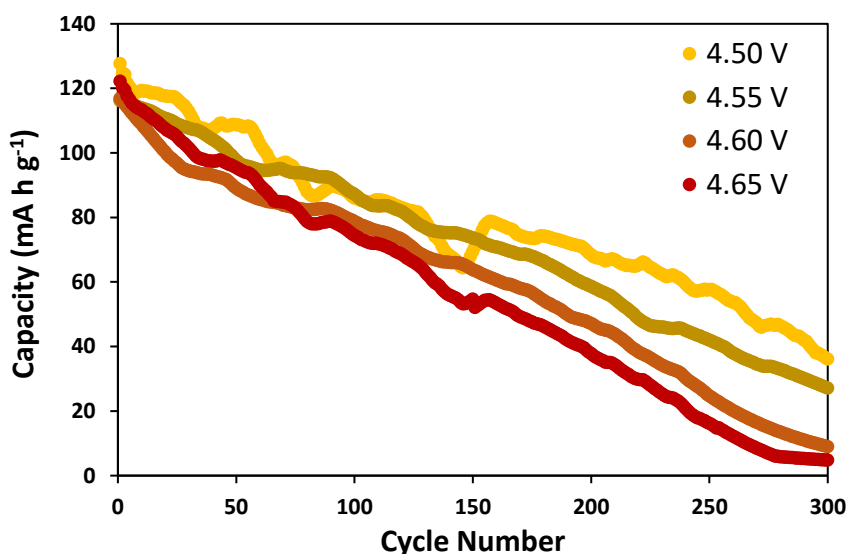


Figure 32: Long-term cycling performance of NaNMC with 5 layers of alucone cycled between 2.0 V and 4.50, 4.55, 4.60, or 4.65 V.

6 Conclusions and Future Work

In summary, the synthesis of $\text{Na}_{0.66}(\text{Ni}_{0.13}\text{Mn}_{0.54}\text{Co}_{0.13})\text{O}_2$ was optimized with regards to temperature and chelating agent to produce a pure highly crystalline cathode material for sodium ion batteries. An annealing temperature of 850 °C and citric acid as the chelating agent produced the best results. Its quality and composition were characterized using XRD, ICP, and SEM. This material was assembled into a cathode and coated with an ultrathin film of alucone using molecular layer deposition. The presence of this coating was verified using TEM and characterized electrochemically using EIS and battery cycling at various rates and voltage ranges.

Five layers of alucone on the NaNMC material resulted in the best performance at nearly all stages of electrochemical characterization. The 5-layer sample had a capacity of 93 mA h g⁻¹ after 100 cycles while the uncoated sample had a capacity of 78 mA h g⁻¹ and the 10-layer and 20-layer had a similar capacity fading. Additionally, all coated samples outperformed the pristine sample at rates above 0.5 C indicating the coating's effectiveness at increasing the high-rate performance and the 5-layer sample had the best rate performance. The improvement in performance of the 5-layer coating was verified by EIS spectra which showed less internal resistance than the other samples and no change in resistance after 100 charge/discharge cycles. Conversely, the internal resistance of the uncoated sample increased by 143% after 100 charge/discharge cycles which indicates its instability.

The results were explained by the known ability of a thin flexible coating on battery materials to prevent dissolution of the active material into the electrolyte, prevent side reactions from occurring, and to stabilize the active material by preventing structural changes while accommodating large volume changes. Alucone's softness and flexibility likely contributed to

these effects while deposition by MLD ensured that the coating was uniform and ultrathin. Alucone's higher conductivity also likely played a role in this enhanced performance.

Since this study demonstrated that 10 and 20 layers of alucone had little effect on SIB capacity while 5 layers increased it, it can be concluded that coating thickness plays a vital role. A coating that is too thick decreases the diffusion of ions to and from the electrode surface causing poorer performance. Another conclusion from this phenomenon is that MLD is a critical method for creating these coatings since other methods produce too thick a layer or a non-uniform layer, and a 1 nm difference is enough to decrease performance.

The following research is recommended to expand upon this thesis. First, it is supposed that this alucone coating by MLD would be beneficial to many, if not all, SIB cathode materials. It should be of particular benefit to high-volume-change materials such as Sn or Fe_3O_4 since alucone is more flexible than the conventional metal oxide coatings used to protect such materials. A logical follow-up to this thesis would be to explore the effect of an alucone coating on these other materials.

Second, the effect of increasing the carbon linker length in the alucone should be investigated. A longer carbon linker should increase the flexibility of the coating as well as conductivity. Glycerol was used in this thesis which contains two carbon atoms between each oxygen reaction site, but a longer molecule such as pentane-1,3,5-triol would have more carbon. Similarly, including a double bond in the carbon linker would increase its conductivity. However, the selection of molecules which can be deposited by MLD is severely limited.

Finally, while this thesis determined that 5 layers of alucone resulted in the best electrochemical properties, it also highlighted how much slight changes in coating thickness

affected performance. It would be an appropriate extension of this thesis to investigate the performance of 3- or 7-layer coatings to determine the true maximum.

References

- (1) Manthiram, A. Materials Challenges and Opportunities of Lithium Ion Batteries. *J. Phys. Chem. Lett.* **2011**, *2* (3), 176–184.
- (2) Li, H.; Wang, Z.; Chen, L.; Huang, X. Research on Advanced Materials for Li-Ion Batteries. *Adv. Mater.* **2009**, *21* (45), 4593–4607.
- (3) Whittingham, M. S. Lithium Batteries and Cathode Materials. *Chem. Rev.* **2004**, *104* (10), 4271–4302.
- (4) Xiong, F.; Yan, H. J.; Chen, Y.; Xu, B.; Le, J. X.; Ouyang, C. Y. The Atomic and Electronic Structure Changes Upon Delithiation of LiCoO₂: From First Principles Calculations. *ResearchGate* **2012**, *7* (10), 9390–9400.
- (5) Nitta, N.; Wu, F.; Lee, J. T.; Yushin, G. Li-Ion Battery Materials: Present and Future. *Mater. Today* **2015**, *18* (5), 252–264.
- (6) Padhi, A. K.; Nanjundaswamy, K. S.; Goodenough, J. B. D. Phospho-Olivines as Positive-Electrode Materials for Rechargeable Lithium Batteries. *J. Electrochem. Soc.* **1997**, *144* (4), 1188–1194.
- (7) Bruce, P. G.; Scrosati, B.; Tarascon, J.-M. Nanomaterials for Rechargeable Lithium Batteries. *Angew. Chem. Int. Ed.* **2008**, *47* (16), 2930–2946.
- (8) Thackeray, M. M.; Johnson, P. J.; de Picciotto, L. A.; Bruce, P. G.; Goodenough, J. B. Electrochemical Extraction of Lithium from LiMn₂O₄. *Mater. Res. Bull.* **1984**, *19* (2), 179–187.
- (9) Thackeray, M. M.; David, W. I. F.; Bruce, P. G.; Goodenough, J. B. Lithium Insertion into Manganese Spinel. *Mater. Res. Bull.* **1983**, *18* (4), 461–472.
- (10) Lee, H.-W.; Muralidharan, P.; Ruffo, R.; Mari, C. M.; Cui, Y.; Kim, D. K. Ultrathin Spinel LiMn₂O₄ Nanowires as High Power Cathode Materials for Li-Ion Batteries. *Nano Lett.* **2010**, *10* (10), 3852–3856.
- (11) Ohzuku, T.; Makimura, Y. Layered Lithium Insertion Material of LiCo_{1/3}Ni_{1/3}Mn_{1/3}O₂ for Lithium-Ion Batteries. *Chem. Lett.* **2001**, *30* (7), 642–643.
- (12) Wu, F.; Tan, G.; Lu, J.; Chen, R.; Li, L.; Amine, K. Stable Nanostructured Cathode with Polycrystalline Li-Deficient Li_{0.28}Co_{0.29}Ni_{0.30}Mn_{0.20}O₂ for Lithium-Ion Batteries. *Nano Lett.* **2014**, *14* (3), 1281–1287.
- (13) Ye, J.; Li, Y.; Zhang, L.; Zhang, X.; Han, M.; He, P.; Zhou, H. Fabrication and Performance of High Energy Li-Ion Battery Based on the Spherical Li[Li_{0.2}Ni_{0.16}Co_{0.1}Mn_{0.54}]O₂ Cathode and Si Anode. *ACS Appl. Mater. Interfaces* **2016**, *8* (1), 208–214.

- (14) Hwang, J.-Y.; Myung, S.-T.; Sun, Y.-K. Sodium-Ion Batteries: Present and Future. *Chem. Soc. Rev.* **2017**, *46* (12), 3529–3614.
- (15) Slater, M. D.; Kim, D.; Lee, E.; Johnson, C. S. Sodium-Ion Batteries. *Adv. Funct. Mater.* **2013**, *23* (8), 947–958.
- (16) Croguennec, L.; Palacin, M. R. Recent Achievements on Inorganic Electrode Materials for Lithium-Ion Batteries. *J. Am. Chem. Soc.* **2015**, *137* (9), 3140–3156.
- (17) Hong, K.; Qie, L.; Zeng, R.; Yi, Z.; Zhang, W.; Wang, D.; Yin, W.; Wu, C.; Fan, Q.; Zhang, W. Biomass Derived Hard Carbon Used as a High Performance Anode Material for Sodium Ion Batteries. *J. Mater. Chem. A* **2014**, *2* (32), 12733–12738.
- (18) Ponrouch, A.; Goñi, A. R.; Palacín, M. R. High Capacity Hard Carbon Anodes for Sodium Ion Batteries in Additive Free Electrolyte. *Electrochem. Commun.* **2013**, *27*, 85–88.
- (19) Stevens, D. A.; Dahn, J. R. High Capacity Anode Materials for Rechargeable Sodium-Ion Batteries. *J. Electrochem. Soc.* **2000**, *147* (4), 1271–1273.
- (20) Ellis, B. L.; Nazar, L. F. Sodium and Sodium-Ion Energy Storage Batteries. *Curr. Opin. Solid State Mater. Sci.* **2012**, *16* (4), 168–177.
- (21) Yabuuchi, N.; Kubota, K.; Dahbi, M.; Komaba, S. Research Development on Sodium-Ion Batteries <http://pubs.acs.org/doi/abs/10.1021/cr500192f> (accessed Feb 14, 2018).
- (22) Kim, S.-W.; Seo, D.-H.; Ma, X.; Ceder, G.; Kang, K. Electrode Materials for Rechargeable Sodium-Ion Batteries: Potential Alternatives to Current Lithium-Ion Batteries. *Adv. Energy Mater.* **2012**, *2* (7), 710–721.
- (23) Kubota, K.; Komaba, S. Review—Practical Issues and Future Perspective for Na-Ion Batteries. *J. Electrochem. Soc.* **2015**, *162* (14), A2538–A2550.
- (24) Wang, Y.-X.; Chou, S.-L.; Liu, H.-K.; Dou, S.-X. Reduced Graphene Oxide with Superior Cycling Stability and Rate Capability for Sodium Storage. *Carbon* **2013**, *57*, 202–208.
- (25) Qu, B.; Ma, C.; Ji, G.; Xu, C.; Xu, J.; Meng, Y. S.; Wang, T.; Lee, J. Y. Layered SnS₂-Reduced Graphene Oxide Composite—A High-Capacity, High-Rate, and Long-Cycle Life Sodium-Ion Battery Anode Material. *Adv. Mater.* **2014**, *26* (23), 3854–3859.
- (26) Balogun, M.-S.; Luo, Y.; Qiu, W.; Liu, P.; Tong, Y. A Review of Carbon Materials and Their Composites with Alloy Metals for Sodium Ion Battery Anodes. *Carbon* **2016**, *98*, 162–178.
- (27) Wang, H.; Zhang, Y.; Ang, H.; Zhang, Y.; Tan, H. T.; Zhang, Y.; Guo, Y.; Franklin, J. B.; Wu, X. L.; Srinivasan, M.; et al. A High-Energy Lithium-Ion Capacitor by Integration of a 3D Interconnected Titanium Carbide Nanoparticle Chain Anode with a Pyridine-Derived Porous Nitrogen-Doped Carbon Cathode. *Adv. Funct. Mater.* **2016**, *26* (18), 3082–3093.

- (28) Ai, K.; Liu, Y.; Ruan, C.; Lu, L.; Lu, G. (Max). Sp² C-Dominant N-Doped Carbon Sub-Micrometer Spheres with a Tunable Size: A Versatile Platform for Highly Efficient Oxygen-Reduction Catalysts. *Adv. Mater.* **2013**, *25* (7), 998–1003.
- (29) He, Y.; Xu, P.; Zhang, B.; Du, Y.; Song, B.; Han, X.; Peng, H. Ultrasmall MnO Nanoparticles Supported on Nitrogen-Doped Carbon Nanotubes as Efficient Anode Materials for Sodium Ion Batteries. *ACS Appl. Mater. Interfaces* **2017**, *9* (44), 38401–38408.
- (30) Meng, X.; Zhong, Y.; Sun, Y.; Banis, M. N.; Li, R.; Sun, X. Nitrogen-Doped Carbon Nanotubes Coated by Atomic Layer Deposited SnO₂ with Controlled Morphology and Phase. *Carbon* **2011**, *49* (4), 1133–1144.
- (31) Xie, F.; Zhang, L.; Su, D.; Jaroniec, M.; Qiao, S.-Z. Na₂Ti₃O₇@N-Doped Carbon Hollow Spheres for Sodium-Ion Batteries with Excellent Rate Performance. *Adv. Mater.* **2017**, *29* (24), n/a-n/a.
- (32) Yu, X.-Y.; Hu, H.; Wang, Y.; Chen, H.; Lou, X. W. (David). Ultrathin MoS₂ Nanosheets Supported on N-Doped Carbon Nanoboxes with Enhanced Lithium Storage and Electrocatalytic Properties. *Angew. Chem. Int. Ed.* **2015**, *54* (25), 7395–7398.
- (33) Ding, Y.; Chen, L.; Pan, P.; Du, J.; Fu, Z.; Qin, C.; Wang, F. Nitrogen-Doped Carbon Coated MnO Nanopeapods as Superior Anode Materials for Lithium Ion Batteries. *Appl. Surf. Sci.* **2017**, *422*, 1113–1119.
- (34) Oh, S.-M.; Hwang, J.-Y.; Yoon, C. S.; Lu, J.; Amine, K.; Belharouak, I.; Sun, Y.-K. High Electrochemical Performances of Microsphere C-TiO₂ Anode for Sodium-Ion Battery. *ACS Appl. Mater. Interfaces* **2014**, *6* (14), 11295–11301.
- (35) Wu, L.; Buchholz, D.; Bresser, D.; Chagas, L. G.; Passerini, S. Anatase TiO₂ Nanoparticles for High Power Sodium-Ion Anodes. *J. Power Sources* **2014**, *251*, 379–385.
- (36) Xiong, H.; Slater, M. D.; Balasubramanian, M.; Johnson, C. S.; Rajh, T. Amorphous TiO₂ Nanotube Anode for Rechargeable Sodium Ion Batteries. *J. Phys. Chem. Lett.* **2011**, *2* (20), 2560–2565.
- (37) Xu, Y.; Zhou, M.; Wen, L.; Wang, C.; Zhao, H.; Mi, Y.; Liang, L.; Fu, Q.; Wu, M.; Lei, Y. Highly Ordered Three-Dimensional Ni-TiO₂ Nanoarrays as Sodium Ion Battery Anodes. *Chem. Mater.* **2015**, *27* (12), 4274–4280.
- (38) Usui, H.; Yoshioka, S.; Wasada, K.; Shimizu, M.; Sakaguchi, H. Nb-Doped Rutile TiO₂: A Potential Anode Material for Na-Ion Battery. *ACS Appl. Mater. Interfaces* **2015**, *7* (12), 6567–6573.
- (39) Pan, H.; Lu, X.; Yu, X.; Hu, Y.-S.; Li, H.; Yang, X.-Q.; Chen, L. Sodium Storage and Transport Properties in Layered Na₂Ti₃O₇ for Room-Temperature Sodium-Ion Batteries. *Adv. Energy Mater.* **2013**, *3* (9), 1186–1194.

- (40) Senguttuvan, P.; Rousse, G.; Seznec, V.; Tarascon, J.-M.; Palacin, M. R. Na₂Ti₃O₇: Lowest Voltage Ever Reported Oxide Insertion Electrode for Sodium Ion Batteries. *Chem. Mater.* **2011**, *23* (18), 4109–4111.
- (41) Zhang, N.; Han, X.; Liu, Y.; Hu, X.; Zhao, Q.; Chen, J. 3D Porous γ -Fe₂O₃@ C Nanocomposite as High-Performance Anode Material of Na-Ion Batteries. *Adv. Energy Mater.* **2015**, *5* (5).
- (42) Zhou, G.; Wang, D.-W.; Li, F.; Zhang, L.; Li, N.; Wu, Z.-S.; Wen, L.; Lu, G. Q.; Cheng, H.-M. Graphene-Wrapped Fe₃O₄ Anode Material with Improved Reversible Capacity and Cyclic Stability for Lithium Ion Batteries. *Chem. Mater.* **2010**, *22* (18), 5306–5313.
- (43) Liu, Y.; Cheng, Z.; Sun, H.; Arandiyani, H.; Li, J.; Ahmad, M. Mesoporous Co₃O₄ Sheets/3D Graphene Networks Nanohybrids for High-Performance Sodium-Ion Battery Anode. *J. Power Sources* **2015**, *273*, 878–884.
- (44) Wang, Y.; Su, D.; Wang, C.; Wang, G. SnO₂@ MWCNT Nanocomposite as a High Capacity Anode Material for Sodium-Ion Batteries. *Electrochem. Commun.* **2013**, *29*, 8–11.
- (45) Zhou, X.; Wan, L.-J.; Guo, Y.-G. Binding SnO₂ Nanocrystals in Nitrogen-Doped Graphene Sheets as Anode Materials for Lithium-Ion Batteries. *Adv. Mater.* **2013**, *25* (15), 2152–2157.
- (46) Wang, L.; Zhang, K.; Hu, Z.; Duan, W.; Cheng, F.; Chen, J. Porous CuO Nanowires as the Anode of Rechargeable Na-Ion Batteries. *Nano Res.* **2014**, *7* (2), 199–208.
- (47) Yuan, S.; Huang, X.; Ma, D.; Wang, H.; Meng, F.; Zhang, X. Engraving Copper Foil to Give Large-Scale Binder-Free Porous CuO Arrays for a High-Performance Sodium-Ion Battery Anode. *Adv. Mater.* **2014**, *26* (14), 2273–2279.
- (48) Liu, Y.; Wang, H.; Cheng, L.; Han, N.; Zhao, F.; Li, P.; Jin, C.; Li, Y. TiS₂ Nanoplates: A High-Rate and Stable Electrode Material for Sodium Ion Batteries. *Nano Energy* **2016**, *20*, 168–175.
- (49) Zhang, K.; Park, M.; Zhou, L.; Lee, G.-H.; Shin, J.; Hu, Z.; Chou, S.-L.; Chen, J.; Kang, Y.-M. Cobalt-Doped FeS₂ Nanospheres with Complete Solid Solubility as a High-Performance Anode Material for Sodium-Ion Batteries. *Angew. Chem. Int. Ed.* **2016**, *55* (41), 12822–12826.
- (50) David, L.; Bhandavat, R.; Singh, G. MoS₂/Graphene Composite Paper for Sodium-Ion Battery Electrodes. *ACS Nano* **2014**, *8* (2), 1759–1770.
- (51) Hu, Z.; Wang, L.; Zhang, K.; Wang, J.; Cheng, F.; Tao, Z.; Chen, J. MoS₂ Nanoflowers with Expanded Interlayers as High-Performance Anodes for Sodium-Ion Batteries. *Angew. Chem.* **2014**, *126* (47), 13008–13012.

- (52) Xie, X.; Ao, Z.; Su, D.; Zhang, J.; Wang, G. MoS₂/Graphene Composite Anodes with Enhanced Performance for Sodium-Ion Batteries: The Role of the Two-Dimensional Heterointerface. *Adv. Funct. Mater.* **2015**, *25* (9), 1393–1403.
- (53) Denis, Y. W.; Prikhodchenko, P. V.; Mason, C. W.; Batabyal, S. K.; Gun, J.; Sladkevich, S.; Medvedev, A. G.; Lev, O. High-Capacity Antimony Sulphide Nanoparticle-Decorated Graphene Composite as Anode for Sodium-Ion Batteries. *Nat. Commun.* **2013**, *4*, 2922.
- (54) Kim, Y.; Park, Y.; Choi, A.; Choi, N.-S.; Kim, J.; Lee, J.; Ryu, J. H.; Oh, S. M.; Lee, K. T. An Amorphous Red Phosphorus/Carbon Composite as a Promising Anode Material for Sodium Ion Batteries. *Adv. Mater.* **2013**, *25* (22), 3045–3049.
- (55) Qian, J.; Wu, X.; Cao, Y.; Ai, X.; Yang, H. High Capacity and Rate Capability of Amorphous Phosphorus for Sodium Ion Batteries. *Angew. Chem.* **2013**, *125* (17), 4731–4734.
- (56) Song, J.; Yu, Z.; Gordin, M. L.; Hu, S.; Yi, R.; Tang, D.; Walter, T.; Regula, M.; Choi, D.; Li, X. Chemically Bonded Phosphorus/Graphene Hybrid as a High Performance Anode for Sodium-Ion Batteries. *Nano Lett.* **2014**, *14* (11), 6329–6335.
- (57) Liu, Y.; Xu, Y.; Zhu, Y.; Culver, J. N.; Lundgren, C. A.; Xu, K.; Wang, C. Tin-Coated Viral Nanoforests as Sodium-Ion Battery Anodes. *Acs Nano* **2013**, *7* (4), 3627–3634.
- (58) Xu, Y.; Zhu, Y.; Liu, Y.; Wang, C. Electrochemical Performance of Porous Carbon/Tin Composite Anodes for Sodium-Ion and Lithium-Ion Batteries. *Adv. Energy Mater.* **2013**, *3* (1), 128–133.
- (59) Wang, J.; Eng, C.; Chen-Wiegart, Y. K.; Wang, J. Probing Three-Dimensional Sodiation–desodiation Equilibrium in Sodium-Ion Batteries by in Situ Hard X-Ray Nanotomography. *Nat. Commun.* **2015**, *6* (1).
- (60) Abel, P. R.; Lin, Y.-M.; de Souza, T.; Chou, C.-Y.; Gupta, A.; Goodenough, J. B.; Hwang, G. S.; Heller, A.; Mullins, C. B. Nanocolumnar Germanium Thin Films as a High-Rate Sodium-Ion Battery Anode Material. *J. Phys. Chem. C* **2013**, *117* (37), 18885–18890.
- (61) Wu, L.; Hu, X.; Qian, J.; Pei, F.; Wu, F.; Mao, R.; Ai, X.; Yang, H.; Cao, Y. Sb–C Nanofibers with Long Cycle Life as an Anode Material for High-Performance Sodium-Ion Batteries. *Energy Environ. Sci.* **2014**, *7* (1), 323–328.
- (62) Zhu, Y.; Han, X.; Xu, Y.; Liu, Y.; Zheng, S.; Xu, K.; Hu, L.; Wang, C. Electrospun Sb/C Fibers for a Stable and Fast Sodium-Ion Battery Anode. *ACS Nano* **2013**, *7* (7), 6378–6386.
- (63) Su, D.; Dou, S.; Wang, G. Bismuth: A New Anode for the Na-Ion Battery. *Nano Energy* **2015**, *12*, 88–95.
- (64) Claude, D.; J. Braconnier, J.; Fouassier, C.; Hagenmuller, P. Electrochemical Intercalation of Sodium in Na_xCoO₂ Bronzes. *Solid State Ion.* **1981**, *3–4*, 165–169.

- (65) Zhao, J.; Zhao, L.; Dimov, N.; Okada, S.; Nishida, T. Electrochemical and Thermal Properties of α -NaFeO₂ Cathode for Na-Ion Batteries. *J. Electrochem. Soc.* **2013**, *160* (5), A3077–A3081.
- (66) Ding, J.-J.; Zhou, Y.-N.; Sun, Q.; Fu, Z.-W. Cycle Performance Improvement of NaCrO₂ Cathode by Carbon Coating for Sodium Ion Batteries. *Electrochem. Commun.* **2012**, *22*, 85–88.
- (67) Billaud, J.; Clément, R. J.; Armstrong, A. R.; Canales-Vázquez, J.; Rozier, P.; Grey, C. P.; Bruce, P. G. β -NaMnO₂: A High-Performance Cathode for Sodium-Ion Batteries. *J. Am. Chem. Soc.* **2014**, *136* (49), 17243–17248.
- (68) Clément, R. J.; Bruce, P. G.; Grey, C. P. Manganese-Based P2-Type Transition Metal Oxides as Sodium-Ion Battery Cathode Materials. *J. Electrochem. Soc.* **2015**, *162* (14), A2589–A2604.
- (69) Han, M. H.; Gonzalo, E.; Singh, G.; Rojo, T. A Comprehensive Review of Sodium Layered Oxides: Powerful Cathodes for Na-Ion Batteries. *Energy Environ. Sci.* **2015**, *8* (1), 81–102.
- (70) Vassilaras, P.; Ma, X.; Li, X.; Ceder, G. Electrochemical Properties of Monoclinic NaNiO₂. *J. Electrochem. Soc.* **2013**, *160* (2), A207–A211.
- (71) Yoshida, H.; Yabuuchi, N.; Kubota, K.; Ikeuchi, I.; Garsuch, A.; Schulz-Dobrick, M.; Komaba, S. P2-Type Na_{2/3}Ni_{1/3}Mn_{2/3}–xTi_xO₂ as a New Positive Electrode for Higher Energy Na-Ion Batteries. *Chem. Commun.* **2014**, *50* (28), 3677–3680.
- (72) Wang, H.; Yang, B.; Liao, X.-Z.; Xu, J.; Yang, D.; He, Y.-S.; Ma, Z.-F. Electrochemical Properties of P2-Na_{2/3}[Ni_{1/3}Mn_{2/3}]O₂ Cathode Material for Sodium Ion Batteries When Cycled in Different Voltage Ranges. *Electrochimica Acta* **2013**, *113*, 200–204.
- (73) Yuan, D.; Hu, X.; Qian, J.; Pei, F.; Wu, F.; Mao, R.; Ai, X.; Yang, H.; Cao, Y. P2-Type Na_{0.67}Mn_{0.65}Fe_{0.2}Ni_{0.15}O₂ Cathode Material with High-Capacity for Sodium-Ion Battery. *Electrochimica Acta* **2014**, *116*, 300–305.
- (74) Yu, H.; Guo, S.; Zhu, Y.; Ishida, M.; Zhou, H. Novel Titanium-Based O3-Type NaTi_{0.5}Ni_{0.5}O₂ as a Cathode Material for Sodium Ion Batteries. *Chem. Commun.* **2014**, *50* (4), 457–459.
- (75) Avdeev, M.; Mohamed, Z.; Ling, C. D.; Lu, J.; Tamaru, M.; Yamada, A.; Barpanda, P. Magnetic Structures of NaFePO₄ Maricite and Triphylite Polymorphs for Sodium-Ion Batteries. *Inorg. Chem.* **2013**, *52* (15), 8685–8693.
- (76) Li, S.; Dong, Y.; Xu, L.; Xu, X.; He, L.; Mai, L. Effect of Carbon Matrix Dimensions on the Electrochemical Properties of Na₃V₂(PO₄)₃ Nanograins for High-Performance Symmetric Sodium-Ion Batteries. *Adv. Mater.* **2014**, *26* (21), 3545–3553.

- (77) Ati, M.; Dupont, L.; Recham, N.; Chotard, J. N.; Walker, W. T.; Davoisne, C.; Barpanda, P.; Sarou-Kanian, V.; Armand, M.; Tarascon, J. M. Synthesis, Structural, and Transport Properties of Novel Bihydrated Fluorosulphates $\text{NaMSO}_4\text{F} \cdot 2\text{H}_2\text{O}$ (M= Fe, Co, and Ni). *Chem. Mater.* **2010**, *22* (13), 4062–4068.
- (78) Tripathi, R.; Gardiner, G. R.; Islam, M. S.; Nazar, L. F. Alkali-Ion Conduction Paths in LiFeSO_4F and NaFeSO_4F Tavorite-Type Cathode Materials. *Chem. Mater.* **2011**, *23* (8), 2278–2284.
- (79) Barpanda, P.; Oyama, G.; Ling, C. D.; Yamada, A. Kröhnkite-Type $\text{Na}_2\text{Fe}(\text{SO}_4)_2 \cdot 2\text{H}_2\text{O}$ as a Novel 3.25 V Insertion Compound for Na-Ion Batteries. *Chem. Mater.* **2014**, *26* (3), 1297–1299.
- (80) Hwa, J. Y.; S, C. A.; E, J. R.; Poul, N.; Kyung, K. D. In Situ X-Ray Diffraction Studies on Structural Changes of a P2 Layered Material during Electrochemical Desodiation/Sodiation. *Adv. Funct. Mater.* **2015**, *25* (21), 3227–3237.
- (81) Kaliyappan, K.; Liu, J.; Lushington, A.; Li, R.; Sun, X. Highly Stable $\text{Na}_{2/3}(\text{Mn}_{0.54}\text{Ni}_{0.13}\text{Co}_{0.13})\text{O}_2$ Cathode Modified by Atomic Layer Deposition for Sodium-Ion Batteries. *ChemSusChem* **2015**, *8* (15), 2537–2543.
- (82) Kaliyappan, K.; Liu, J.; Xiao, B.; Lushington, A.; Li, R.; Sham, T.-K.; Sun, X. Enhanced Performance of P2- $\text{Na}_{0.66}(\text{Mn}_{0.54}\text{Co}_{0.13}\text{Ni}_{0.13})\text{O}_2$ Cathode for Sodium-Ion Batteries by Ultrathin Metal Oxide Coatings via Atomic Layer Deposition. *Adv. Funct. Mater.* **2017**, *27* (37).
- (83) Xu, J.; Lee, D. H.; Clément, R. J.; Yu, X.; Leskes, M.; Pell, A. J.; Pintacuda, G.; Yang, X.-Q.; Grey, C. P.; Meng, Y. S. Identifying the Critical Role of Li Substitution in $\text{P2-Na}_x[\text{Li}_y\text{Ni}_z\text{Mn}_{1-y-z}]\text{O}_2$ ($0 < X, Y, Z < 1$) Intercalation Cathode Materials for High-Energy Na-Ion Batteries. *Chem. Mater.* **2014**, *26* (2), 1260–1269.
- (84) Singh, G.; Tapia-Ruiz, N.; Lopez del Amo, J. M.; Maitra, U.; Somerville, J. W.; Armstrong, A. R.; Martinez de Ilarduya, J.; Rojo, T.; Bruce, P. G. High Voltage Mg-Doped $\text{Na}_{0.67}\text{Ni}_{0.3-x}\text{Mg}_x\text{Mn}_{0.7}\text{O}_2$ ($X = 0.05, 0.1$) Na-Ion Cathodes with Enhanced Stability and Rate Capability. *Chem. Mater.* **2016**, *28* (14), 5087–5094.
- (85) Wu, X.; Xu, G.-L.; Zhong, G.; Gong, Z.; McDonald, M. J.; Zheng, S.; Fu, R.; Chen, Z.; Amine, K.; Yang, Y. Insights into the Effects of Zinc Doping on Structural Phase Transition of P2-Type Sodium Nickel Manganese Oxide Cathodes for High-Energy Sodium Ion Batteries. *ACS Appl. Mater. Interfaces* **2016**, *8* (34), 22227–22237.
- (86) Buchholz, D.; Moretti, A.; Kloepsch, R.; Nowak, S.; Siozios, V.; Winter, M.; Passerini, S. Toward Na-Ion Batteries—Synthesis and Characterization of a Novel High Capacity Na Ion Intercalation Material. *Chem. Mater.* **2013**, *25* (2), 142–148.
- (87) Lu, Z.; Dahn, J. R. In Situ X-Ray Diffraction Study of P 2 - $\text{Na}_{2/3}[\text{Ni}_{1/3}\text{Mn}_{2/3}]\text{O}_2$. *J. Electrochem. Soc.* **2001**, *148* (11), A1225–A1229.

- (88) Sathiya, M.; Hemalatha, K.; Ramesha, K.; Tarascon, J.-M.; Prakash, A. S. Synthesis, Structure, and Electrochemical Properties of the Layered Sodium Insertion Cathode Material: $\text{NaNi}_{1/3}\text{Mn}_{1/3}\text{Co}_{1/3}\text{O}_2$. *Chem. Mater.* **2012**, *24* (10), 1846–1853.
- (89) Yuan, D.; He, W.; Pei, F.; Wu, F.; Wu, Y.; Qian, J.; Cao, Y.; Ai, X.; Yang, H. Synthesis and Electrochemical Behaviors of Layered $\text{Na}_{0.67}[\text{Mn}_{0.65}\text{Co}_{0.2}\text{Ni}_{0.15}]\text{O}_2$ Microflakes as a Stable Cathode Material for Sodium-Ion Batteries. *J. Mater. Chem. A* **2013**, *1* (12), 3895–3899.
- (90) Komaba, S.; Yabuuchi, N.; Nakayama, T.; Ogata, A.; Ishikawa, T.; Nakai, I. Study on the Reversible Electrode Reaction of $\text{Na}_{1-x}\text{Ni}_{0.5}\text{Mn}_{0.5}\text{O}_2$ for a Rechargeable Sodium-Ion Battery. *Inorg. Chem.* **2012**, *51* (11), 6211–6220.
- (91) Ding, J.-J.; Zhou, Y.-N.; Sun, Q.; Fu, Z.-W. Cycle Performance Improvement of NaCrO_2 Cathode by Carbon Coating for Sodium Ion Batteries. *Electrochem. Commun.* **2012**, *22*, 85–88.
- (92) Ellis, B. L.; Makahnouk, W. R. M.; Makimura, Y.; Toghiani, K.; Nazar, L. F. A Multifunctional 3.5 V Iron-Based Phosphate Cathode for Rechargeable Batteries. *Nat. Mater.* **2007**, *6* (10), 749–753.
- (93) Jian, Z.; Zhao, L.; Pan, H.; Hu, Y.-S.; Li, H.; Chen, W.; Chen, L. Carbon Coated $\text{Na}_3\text{V}_2(\text{PO}_4)_3$ as Novel Electrode Material for Sodium Ion Batteries. *Electrochem. Commun.* **2012**, *14* (1), 86–89.
- (94) Ritala, M.; Leskelä, M. Atomic Layer Deposition. In *Handbook of Thin Films*; Elsevier, 2002; pp 103–159.
- (95) Li, X.; Liu, J.; Meng, X.; Tang, Y.; Banis, M. N.; Yang, J.; Hu, Y.; Li, R.; Cai, M.; Sun, X. Significant Impact on Cathode Performance of Lithium-Ion Batteries by Precisely Controlled Metal Oxide Nanocoatings via Atomic Layer Deposition. *J. Power Sources* **2014**, *247*, 57–69.
- (96) Wang, D.; Yang, J.; Liu, J.; Li, X.; Li, R.; Cai, M.; Sham, T.-K.; Sun, X. Atomic Layer Deposited Coatings to Significantly Stabilize Anodes for Li Ion Batteries: Effects of Coating Thickness and the Size of Anode Particles. *J. Mater. Chem. A* **2014**, *2* (7), 2306–2312.
- (97) Li, X.; Liu, J.; Wang, B.; Banis, M. N.; Xiao, B.; Li, R.; Sham, T.-K.; Sun, X. Nanoscale Stabilization of Li–sulfur Batteries by Atomic Layer Deposited Al_2O_3 . *RSC Adv.* **2014**, *4* (52), 27126–27129.
- (98) Li, X.; Liu, J.; Banis, M. N.; Lushington, A.; Li, R.; Cai, M.; Sun, X. Atomic Layer Deposition of Solid-State Electrolyte Coated Cathode Materials with Superior High-Voltage Cycling Behavior for Lithium Ion Battery Application. *Energy Environ. Sci.* **2014**, *7* (2), 768–778.

- (99) Liu, J.; Banis, M. N.; Li, X.; Lushington, A.; Cai, M.; Li, R.; Sham, T.-K.; Sun, X. Atomic Layer Deposition of Lithium Tantalate Solid-State Electrolytes. *J. Phys. Chem. C* **2013**, *117* (39), 20260–20267.
- (100) Li, X.; Meng, X.; Liu, J.; Geng, D.; Zhang, Y.; Banis, M. N.; Li, Y.; Yang, J.; Li, R.; Sun, X.; et al. Tin Oxide with Controlled Morphology and Crystallinity by Atomic Layer Deposition onto Graphene Nanosheets for Enhanced Lithium Storage. *Adv. Funct. Mater.* **2012**, *22* (8), 1647–1654.
- (101) Snyder, M. Q.; Trebukhova, S. A.; Ravdel, B.; Wheeler, M. C.; DiCarlo, J.; Tripp, C. P.; DeSisto, W. J. Synthesis and Characterization of Atomic Layer Deposited Titanium Nitride Thin Films on Lithium Titanate Spinel Powder as a Lithium-Ion Battery Anode. *J. Power Sources* **2007**, *165* (1), 379–385.
- (102) Han, X.; Liu, Y.; Jia, Z.; Chen, Y.-C.; Wan, J.; Weadock, N.; Gaskell, K. J.; Li, T.; Hu, L. Atomic-Layer-Deposition Oxide Nanoglue for Sodium Ion Batteries. *Nano Lett.* **2014**, *14* (1), 139–147.
- (103) Lee Byoung H.; Yoon Byunghoon; Abdulagatov Aziz I.; Hall Robert A.; George Steven M. Growth and Properties of Hybrid Organic-Inorganic Metalcone Films Using Molecular Layer Deposition Techniques. *Adv. Funct. Mater.* **2012**, *23* (5), 532–546.
- (104) Lee, B. H.; Yoon, B.; Anderson, V. R.; George, S. M. Alucone Alloys with Tunable Properties Using Alucone Molecular Layer Deposition and Al₂O₃ Atomic Layer Deposition. *J. Phys. Chem. C* **2012**, *116* (5), 3250–3257.
- (105) Piper, D. M.; Travis, J. J.; Young, M.; Son, S.-B.; Kim, S. C.; Oh, K. H.; George, S. M.; Ban, C.; Lee, S.-H. Reversible High-Capacity Si Nanocomposite Anodes for Lithium-Ion Batteries Enabled by Molecular Layer Deposition. *Adv. Mater.* **2014**, *26* (10), 1596–1601.
- (106) He, Y.; Piper, D. M.; Gu, M.; Travis, J. J.; George, S. M.; Lee, S.-H.; Genc, A.; Pullan, L.; Liu, J.; Mao, S. X.; et al. In Situ Transmission Electron Microscopy Probing of Native Oxide and Artificial Layers on Silicon Nanoparticles for Lithium Ion Batteries. *ACS Nano* **2014**, *8* (11), 11816–11823.
- (107) Li, X.; Lushington, A.; Sun, Q.; Xiao, W.; Liu, J.; Wang, B.; Ye, Y.; Nie, K.; Hu, Y.; Xiao, Q.; et al. Safe and Durable High-Temperature Lithium–Sulfur Batteries via Molecular Layer Deposited Coating. *Nano Lett.* **2016**, *16* (6), 3545–3549.
- (108) Luo, L.; Yang, H.; Yan, P.; Travis, J. J.; Lee, Y.; Liu, N.; Molina Piper, D.; Lee, S.-H.; Zhao, P.; George, S. M.; et al. Surface-Coating Regulated Lithiation Kinetics and Degradation in Silicon Nanowires for Lithium Ion Battery. *ACS Nano* **2015**, *9* (5), 5559–5566.
- (109) Li, X.; Lushington, A.; Liu, J.; Li, R.; Sun, X. Superior Stable Sulfur Cathodes of Li–S Batteries Enabled by Molecular Layer Deposition. *Chem. Commun.* **2014**, *50* (68), 9757–9760.

- (110) BraggsLaw https://serc.carleton.edu/research_education/geochemsheets/BraggsLaw.html (accessed May 8, 2018).
- (111) Amin, D. G. ZnO and CuO Nanostructures: Low Temperature Growth, Characterization, Their Optoelectronic and Sensing Applications. **2018**.
- (112) Zavalis, T. Studying Impedance to Analyze the Li-Ion Battery with an App. *COMSOL Multiphysics*©. <https://www.comsol.com/blogs/studying-impedance-to-analyze-the-li-ion-battery-with-an-app/> (accessed May 9, 2018).
- (113) Aziz, N. A. A.; Abdullah, T. K.; Mohamad, A. A. Synthesis of LiCoO₂ Prepared by Sol-gel Method. *Procedia Chem.* **2016**, *19*, 861–864.
- (114) Ban, C.; George, S. M. Molecular Layer Deposition for Surface Modification of Lithium-Ion Battery Electrodes. *Adv. Mater. Interfaces* **2016**, *3* (21).